The Dissertation Committee for Pratik Prakash Donde
certifies that this is the approved version of the following dissertation:

LES/PDF approach for turbulent reacting flows

Committee:

Venkat Raman, Supervisor

Noel Clemens

Ofodike Ezekoye

David Goldstein

Robert Moser

LES/PDF approach for turbulent reacting flows

by

Pratik Prakash Donde, B.E.; M.Tech.

DISSERTATION

Presented to the Faculty of the Graduate School of

The University of Texas at Austin

in Partial Fulfillment

of the Requirements

for the Degree of

DOCTOR OF PHILOSOPHY

THE UNIVERSITY OF TEXAS AT AUSTIN

December 2012

Dedicated to Sushma, Mamma, and Pratima.

Acknowledgments

I would first like to thank my advisor Prof. Venkat Raman for providing invaluable support and inspiration throughout my PhD studies. Although there are several aspects of his advising that have helped me, I particularly want to mention his emphasis to present in conferences, which motivated me to work hard, and significantly improved the quality of my research.

Next, I wish to thank my wife Sushma who has been my best friend throughout my PhD. She has also been a great mentor, encouraging me to perform to the best of my abilities, and her constant support and motivation has helped me during my most difficult struggles.

I would also like to thank my colleagues in the Department of Aerospace Engineering, with whom I had several valuable discussions. In particular, I want to mention Heeseok Koo, with whom I have co-authored several of my research publications. I also owe my gratitude to anonymous reviewers from Journal of Computational Physics whose constructive criticism helped me in developing the SeQMOM approach.

Finally, I wish to thank NASA and US Department of Defense for funding my research.

LES/PDF approach for turbulent reacting flows

Pratik Prakash Donde, Ph.D.
The University of Texas at Austin, 2012

Supervisor: Venkat Raman

The probability density function (PDF) approach is a powerful technique for large eddy simulation (LES) based modeling of turbulent reacting flows. In this approach, the joint-PDF of all reacting scalars is estimated by solving a PDF transport equation, thus providing detailed information about small-scale correlations between these quantities. The objective of this work is to further develop the LES/PDF approach for studying flame stabilization in supersonic combustors, and for soot modeling in turbulent flames.

Supersonic combustors are characterized by strong shock-turbulence interactions which preclude the application of conventional Lagrangian stochastic methods for solving the PDF transport equation. A viable alternative is provided by quadrature based methods which are deterministic and Eulerian. In this work, it is first demonstrated that the numerical errors associated with LES require special care in the development of PDF solution algorithms. The direct quadrature method of moments (DQMOM) is one quadrature-based approach developed for supersonic combustion modeling. This approach is

shown to generate inconsistent evolution of the scalar moments. Further, gradient-based source terms that appear in the DQMOM transport equations are severely underpredicted in LES leading to artificial mixing of fuel and oxidizer. To overcome these numerical issues, a new approach called semi-discrete quadrature method of moments (SeQMOM) is formulated. The performance of the new technique is compared with the DQMOM approach in canonical flow configurations as well as a three-dimensional supersonic cavity stabilized flame configuration. The SeQMOM approach is shown to predict subfilter statistics accurately compared to the DQMOM approach.

For soot modeling in turbulent flows, an LES/PDF approach is integrated with detailed models for soot formation and growth. The PDF approach directly evolves the joint statistics of the gas-phase scalars and a set of moments of the soot number density function. This LES/PDF approach is then used to simulate a turbulent natural gas flame. A Lagrangian method formulated in cylindrical coordinates solves the high dimensional PDF transport equation and is coupled to an Eulerian LES solver. The LES/PDF simulations show that soot formation is highly intermittent and is always restricted to the fuel-rich region of the flow. The PDF of soot moments has a wide spread leading to a large subfilter variance. Further, the conditional statistics of soot moments conditioned on mixture fraction and reaction progress variable show strong correlation between the gas phase composition and soot moments.

Table of Contents

List of Tables

List of Figures

Chapter 1

Introduction

Turbulent reacting flows are encountered in several engineering applications, and their analysis is necessary for design and development of practical engineering devices. These flows are characterized by spatial and temporal fluctuations in the flow field and display a spectrum of length scales, making their study difficult. The presence of chemical reactions further increases the complexity by coupling flow behavior to heat release that occurs at very small length scales.

The objective of this work is development of predictive computational tools for studying two distinct problems involving turbulent combustion. The first involves flame stabilization in supersonic combustors, while the second problem concerns soot formation. In this chapter, a brief background of these problems of interest is first provided. This is followed by an introduction to large eddy simulation (LES)/ probability density function (PDF) based computational modeling of turbulent reacting flows. Finally, an outline of the dissertation is presented.

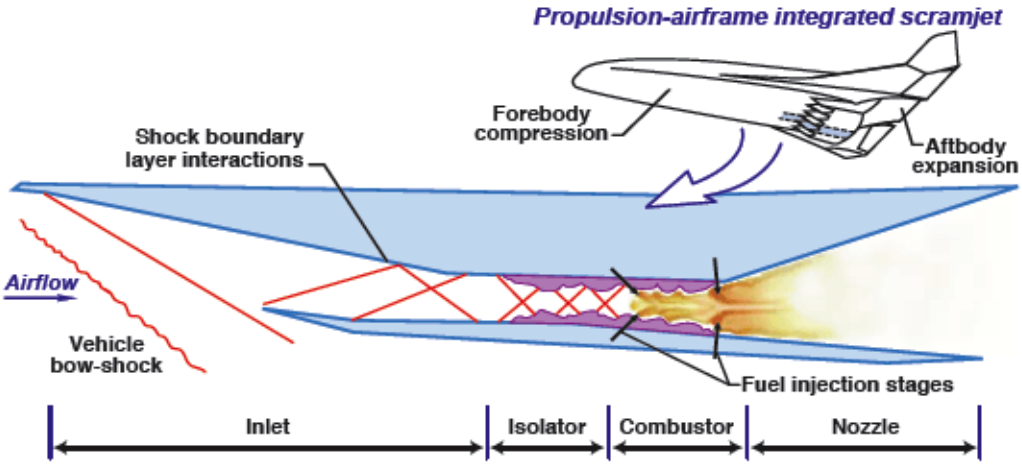

Figure 1.1: Schematic of a scramjet engine [1]. Major components of the engine have been clearly marked.

1.1 Supersonic combustion

Hypersonic air-breathing aircraft employ a propulsion-integrated airframe design, wherein complex shock structures are employed for compressing the air. For generating net positive thrust at extremely high speeds, total pressure losses are minimized by using supersonic combustion ramjet (scramjet) engines wherein the internal flow is supersonic throughout the engine. Figure 1.1 shows a schematic of a scramjet identifying major components.

Stable and robust supersonic combustors are critical for design and development of scramjet engines. Since these combustors have mean velocities that are greater than the speed of sound, the residence time for fuel particles is extremely short, and is of the order of milliseconds. Also, supersonic combustors are characterized by shocks, and shock-combustion-turbulent boundary

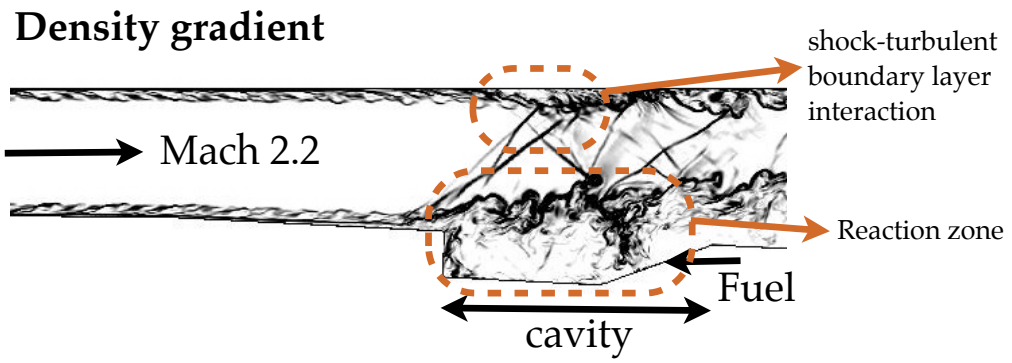

Figure 1.2: Instantaneous density gradient contours for a Mach 2.2 cavity-based supersonic combustor [12].

layer interactions that lead to high total pressure losses. Special design features are therefore required for ensuring adequate mixing and reactivity, so that acceptable combustion efficiencies can be obtained while maintaining low total pressure losses due to shocks and boundary layers.

For attaining these objectives, several designs have been employed. The simplest of these designs uses a jet-in-supersonic crossflow configuration for fuel injection, which accelerates fuel jet breakdown, leading to faster small scale mixing of fuel and oxidizer [2–5]. The injection of a fuel jet into a supersonic crossflow leads to a strong bow shock at the interface of the two streams, which creates boundary layer separation upstream of the fuel injector. The resulting subsonic recirculation bubble provides longer residence times, and the increase in static temperature in the near-wall region increases fuel reactivity, leading to a stable reaction zone required for fuel-air mixing and ignition.

Although transverse jets could be used as stand-alone injection designs [6–8], other approaches that use an upstream step [9,10] or a cavity [5,11] have been considered in order to reduce the pressure losses associated with jet-based injection. For instance, figure 1.2 shows density gradient contours for a Mach 2.2 cavity-based combustor. This combustor was designed and studied experimentally at United Technologies Research Center [12], and includes hydrocarbon fuel injected within the cavity. Note that in spite of the cavity configuration, strong shocks are present within the combustor, and combustion-based instabilities can lead to drastic changes in the shock-structure potentially leading to extinction. Consequently, a fundamental understanding of the flow and reaction structures within supersonic combustors is necessary for the design of reliable scramjet engines.

1.2 Soot formation

Soot particles are carbon compounds formed due to incomplete combustion of hydrocarbon fuels, and are classified as particulate matter. Figure 1.3 shows an experimental piloted natural gas flame. Soot particles in this flame are formed beyond 50 jet diameters, and are indicated by the radiating part of this flame. In addition to adversely affecting the environment, soot particles are also know carcinogens and can cause several respiratory problems in humans. Consequently, there is a significant motivation for reducing soot emissions from aircraft and automobile engines.

Soot formation inside turbulent combustors is a highly unsteady pro-

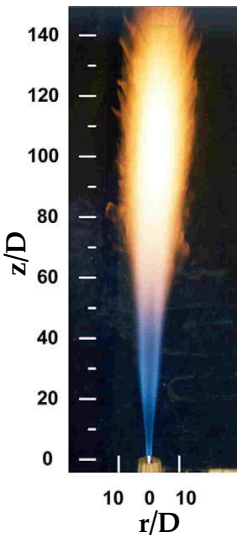

Figure 1.3: An experimental turbulent flame producing soot [13].

cess, and is typically characterized by soot production in fuel-rich high temperature regions of the flow, followed by oxidation and the corresponding destruction of soot after dilution with air. The amount of soot emitted is the result of the differences between these generation and oxidation processes. More importantly, the generation and oxidation processes are not continuous and occur with very high intermittency, indicating that the temporal history of soot precursors, turbulence-related strain, and combustion processes are critical in determining emission levels. A fundamental understanding of these processes is therefore necessary for development of efficient and clean combustors.

1.3 Modeling turbulent reacting flows

Study of turbulent reacting flows discussed above poses a tremendous challenge. Nonetheless, partly due to increasing computational power, significant progress has been made in understanding these flows using computational fluid dynamics (CFD). Turbulent fluid flow is governed by the Navier-Stokes (NS) equations [14, 15], and a numerical solution to these equations leads to the area of CFD. The most comprehensive approach in CFD is direct numerical simulation (DNS) in which discretized NS equations are solved on a computational grid. In DNS all scales of the flow field are resolved, resulting in extremely detailed data sets. The size of the smallest scales in the flow however, reduces with Reynolds number and as a result, the high computational cost associated with DNS of flows with even moderate Reynolds numbers precludes its application in practical engineering configurations. Nonetheless, DNS of canonical configurations is useful for fundamental studies, and for model development and validation [16–21].

For practical configurations, the large eddy simulation (LES) methodology offers a viable alternative. Note that in DNS, 99% of the computational effort is spent in resolving the small dissipative scales [14, 22]. Therefore, in LES, large scale features of the flow are resolved, while models are used for representing the effect of small scales. A filtering operation separates the resolved (or filtered) scales and the unresolved scales. As a result of this, energy containing large scales of the flow are accurately captured, making LES well suited for studying processes like mixing, and hence chemically reacting flows [23].

Nonetheless, models are required for subfilter turbulent stresses and chemical reactions.

Combustion models for LES require subfilter correlations of the thermochemical composition state-vector used for describing the chemical reactions. These correlations are represented in terms of a one-point one-time joint probability density function (PDF) of this state vector. Depending on the combustion model, this PDF could potentially be prescribed using an assumed shape. For instance, in the steady laminar flamelet (SLF) approach [24, 25], the thermochemical composition space is parameterized by a conserved scalar called mixture fraction and its dissipation rate. The marginal-PDF of mixture fraction is assumed to be a beta-function [26], while a delta-function is used for describing the conditional-PDF of dissipation rate. This approach towards modeling turbulence-chemistry interactions is computationally inexpensive since the joint-PDF is completely specified using only lower moments of the PDF. Consequently, SLF based studies have been successfully employed for studying several turbulent flame configurations [27–30] where chemistry is fast and highly turbulent phenomenon like extinction are not present.

For more complex flows, reacting scalars need to be included. It should be noted that the shape of the PDF for reactive scalars is problem dependent and cannot be prescribed *a priori*. As a result, in problems involving slow chemistry, or in high Mach number flows, the joint-PDF of the thermochemical composition vector needs to be estimated in each computational cell by solving a PDF transport equation. The corresponding approach leads to LES/PDF

methods for turbulent reacting flows.

1.4 Objective

In this work, computational tools based on the LES/PDF approach have been developed for studying the two problems discussed in Sec. 1.1 and 1.2. Flame stabilization in supersonic combustors is characterized by strong shock-turbulence-chemistry interactions. While the LES/PDF approach is well suited for describing these subfilter correlations, existing methods for estimating the PDF were found to be inaccurate. Consequently, a novel approach for solving the PDF transport equation has been developed for application in shock-containing flows. Soot modeling in turbulent flames on the other hand, involves complex interactions between the gas-phase composition, soot particles and the turbulent flow field. Subfilter interactions arising from chemical reactions and soot particle dynamics are important, and have been modeled using the PDF formulation.

1.5 Outline

Based on this framework, the outline of the dissertation is as follows. Chapter 2 introduces the governing equations for the LES/PDF approach. The PDF approach for supersonic combustion modeling is reviewed in Chapter 3, and errors introduced by existing methods are discussed. A new approach called semi-discrete quadrature method of moments (SeQMOM) is then developed. In Chapter 4, this new approach is used for studying several config-

urations including a supersonic cavity stabilized combustor. Next, Chapter 5 focuses on the problem of soot modeling in turbulent flames, and the corresponding processes and models involved are discussed. In Chapter 6, numerical results for a piloted sooting flame are presented with emphasis on the subfilter correlations between soot and gas-phase. Finally, conclusion are presented in Chapter 7.

Chapter 2

The LES/PDF approach

The PDF approach provides a comprehensive description of small-scale correlations between reacting scalars. In this chapter, governing equations for reacting scalars are first described. This is followed by a discussion of transport equations solved in LES. Finally, the PDF approach for turbulent reacting flows is introduced.

2.1 Composition and enthalpy transport equations

In chemically reacting flows, transport equations need to be solved for a state-vector which represents all reacting scalars. In flows involving purely gas-phase combustion, this state-vector is the gas-phase thermochemical composition vector $\boldsymbol{\phi}$. When detailed chemistry models are used for representing chemical kinetics, $\boldsymbol{\phi}$ includes N_s species mass fractions and enthalpy, where N_s is the number of species present in the chemistry model. On the other hand, when flamelet-based models are used, $\boldsymbol{\phi}$ includes variables used for tabulating chemistry. For the detailed chemistry formulation, transport equations for species mass fractions and enthalpy are as follows [31, 32]:

$$\frac{\partial \rho \phi_\alpha}{\partial t} + \nabla \cdot \rho \mathbf{u} \phi_\alpha = \nabla \cdot \rho D_\alpha \nabla \phi_\alpha + \rho S_\alpha(\boldsymbol{\phi}) \tag{2.1}$$

$$\frac{\partial \rho \phi_h}{\partial t} + \nabla \cdot \rho \mathbf{u} \phi_h = \nabla \cdot \rho D_{th} \nabla \phi_h + \rho S_h(\boldsymbol{\phi}) + \frac{Dp}{Dt} + \boldsymbol{\tau} : \mathbf{S} + A(\boldsymbol{\phi}) \qquad (2.2)$$

Here, $\phi_h = \int_{T_0}^{T} C_p dT$ is the sensible enthalpy, C_p is the specific heat of the gas at constant pressure, and T is the temperature. D_α is the diffusivity of the α^{th} specie, and D_{th} is the thermal diffusivity defined as $D_{th} = K/\rho C_p$, where K is the thermal conductivity of the fluid. In Eq. 2.2, Dp/Dt and $\boldsymbol{\tau} : \mathbf{S}$ represent pressure derivative and viscous dissipation, while $A(\boldsymbol{\phi})$ represents differential diffusivity effects. Specifically,

$$A(\boldsymbol{\phi}) = \nabla \cdot \left(\left[1 - \frac{1}{C_p} \sum \frac{\phi_\alpha C_{p,\alpha}}{Le_\alpha} \right] K \nabla T + \rho \sum \left[(D_\alpha - D_{th}) \nabla C_{p,\alpha} \phi_\alpha T \right] \right), \qquad (2.3)$$

where $C_{p,\alpha}$ and $Le_\alpha = D_{th}/D_\alpha$ are specific heat, and the Lewis number corresponding to the α^{th} specie. Note that $\sum C_{p.\alpha} \phi_\alpha T = \phi_h$. In Eq. 2.3, $A(\boldsymbol{\phi}) \to 0$ as $Le \to 1$. In the remainder of this work, the unity Lewis number assumption is used such that $D_\alpha = D_{th} = D$.

2.2 LES of reacting flows

In LES, equations for the large scale turbulent motions are formulated by filtering the underlying Navier-Stokes equations [14]. The filtering operation for any three-dimensional field Q is written as

$$\widetilde{Q}(\mathbf{x}, t) = \frac{1}{\overline{\rho}} \int \rho(\mathbf{y}, t) Q(\mathbf{y}, t) G(\mathbf{x} - \mathbf{y}) d\mathbf{y}, \qquad (2.4)$$

where $\widetilde{Q}$ is the Favre filtered Q field, ρ denotes the density field, and $\overline{\rho}$ denotes the filtered density field. The filtering kernel, G, would ideally remove

all small scale information from the Q field. The filter kernel also contains a parameter, Δ, which is the filter width or a characteristic length scale. All scales smaller than the filter width, also termed as subfilter scales, have to be modeled explicitly. Applying this filtering procedure to the flow equations, and assuming that the filtering operator commutes with the differentiation operator, the resulting equations governing conservation of mass and momentum are as follows:

$$\frac{\partial \overline{\rho}}{\partial t} + \nabla \cdot \overline{\rho}\widetilde{\mathbf{u}} = 0, \tag{2.5}$$

$$\frac{\partial \overline{\rho}\widetilde{\mathbf{u}}}{\partial t} + \nabla \cdot (\overline{\rho}\widetilde{\mathbf{u}}\widetilde{\mathbf{u}} + \overline{p}\delta - \widetilde{\boldsymbol{\tau}}) + \nabla \cdot \mathcal{M}^{\mathbf{u}} = 0, \tag{2.6}$$

Here $\widetilde{\mathbf{u}}$ is the velocity vector. The viscous stress tensor $\widetilde{\boldsymbol{\tau}} = \widetilde{\mu}(2\widetilde{\mathbf{S}}) + (\widetilde{\beta} - 2/3\widetilde{\mu})\left(\nabla \cdot \widetilde{\mathbf{U}}\right)\delta$, where $\widetilde{\mu}$ is the dynamic viscosity, $\widetilde{\beta}$ is the bulk viscosity, $\overline{p}$ is the pressure, $\widetilde{\mathbf{S}}$ is the strain rate tensor, and δ is the identity tensor. $\mathcal{M}^{\mathbf{u}}$ is the modeled term in the momentum equation and is encountered when filtering operation is applied to the non-linear convection term. This term represents the effect of sub-filter turbulent stresses, and is closed using a Smagorinsky eddy-viscosity model. Specifically,

$$\mathcal{M}^{\mathbf{u}} = \overline{\rho}\left(\widetilde{\mathbf{u}\mathbf{u}} - \widetilde{\mathbf{u}}\widetilde{\mathbf{u}}\right),$$

$$\mathcal{M}^{u}_{ij} - \frac{1}{3}\delta_{ij}\mathcal{M}^{u}_{kk} = -2\mu_t\left(\widetilde{S_{ij}} - \frac{1}{3}\delta_{ij}\widetilde{S_{kk}}\right), \tag{2.7}$$

where $\mathcal{M}^{u}_{ij}$ and $\widetilde{S_{ij}}$ are each components of subfilter stress and filtered strain rate tensor, and turbulent viscosity $\mu_t = C_s\overline{\rho}\Delta^2|\widetilde{\mathbf{S}}|$. A dynamic model [33] is used for determining the value of modeling constant C_s.

Further, the following filtered form of Eq. (2.1) and (2.2) is solved:

$$\frac{\partial \overline{\rho}\widetilde{\phi_h}}{\partial t} + \nabla \cdot \left(\overline{\rho}\widetilde{\mathbf{u}}\widetilde{\phi_h} - \overline{\rho} D_h \nabla \widetilde{\phi_h} \right) - \left(\frac{D\overline{p}}{Dt} + \widetilde{\boldsymbol{\tau}} : \widetilde{\mathbf{S}} + \overline{\rho}\widetilde{S_h(\boldsymbol{\phi})} \right) + \nabla \cdot \mathcal{M}^h = 0, \tag{2.8}$$

$$\frac{\partial \overline{\rho}\widetilde{\phi}_\alpha}{\partial t} + \nabla \cdot \left(\overline{\rho}\widetilde{\mathbf{u}}\widetilde{\phi}_\alpha - D_\alpha \nabla \widetilde{\phi}_\alpha \right) - \overline{\rho}\widetilde{S_\alpha(\boldsymbol{\phi})} + \nabla \cdot \mathcal{M}^{\phi_\alpha} = 0, \tag{2.9}$$

$\mathcal{M}^h$ and M^ϕ_α are modeled terms in the enthalpy and species transport equations resulting from filtering the non-linear convection term. In Eq. 2.8, $D\overline{p}/Dt$ and $\widetilde{\boldsymbol{\tau}} : \widetilde{\mathbf{S}}$ represent pressure derivative and viscous dissipation. Subfilter correlations arising from these quantities have been neglected [34–36]. Note that in problems involving reactions with solid-phase particles like soot or nanoparticles, additional scalars that describe the appropriate number density functions (NDF) need to be accounted for [37–40]. As discussed later in Chapter 5, governing equations for these scalars have a form similar to Eq. 2.9, and therefore the discussion that follows here is directly applicable to the above problems as well.

In the context of combustion modeling, the primary issue is the closure of the chemical source term $\widetilde{\mathbf{S}(\boldsymbol{\phi})}$ in Eq. (2.8) and (2.9). The filtered chemical source term cannot be accurately computed using the filtered scalar values. Instead, the approach used here is to describe the subfilter distribution of the scalars using a one-point one-time joint PDF of $\boldsymbol{\phi}$. The PDF approach is discussed next.

2.3 PDF approach for combustion modeling

The PDF is defined as a mass density function [41–44] as follows:

$$\overline{\rho}(\mathbf{x},t) = \int F(\boldsymbol{\psi};\mathbf{x},t)d\boldsymbol{\psi}, \tag{2.10}$$

where F stands for the one-time one-point PDF. $\boldsymbol{\psi}$ denotes the sample space variables corresponding to the random state vector $\boldsymbol{\phi}$. The moments of the PDF provide filtered moments of the scalar composition. For instance,

$$\widetilde{\phi_\alpha^q \phi_\beta^r} = \frac{1}{\overline{\rho}} \int \psi_\alpha^q \psi_\beta^r F d\boldsymbol{\psi}, \tag{2.11}$$

where α and β denote components of $\boldsymbol{\phi}$. The main advantage of this technique is that the chemical source term, which is a complex and non-linear function of the composition vector and temperature, can be expressed without any modeling. Similar to Eq. 2.11, the filtered chemical source term could be computed by convolution with the PDF. Since the PDF itself is a function of space and time, and is highly problem dependent, it needs to be evolved along with the LES flow equations by solving a PDF transport equation.

2.3.1 The modeled PDF transport equation

A detailed derivation of the transport equation for the joint-PDF of $\boldsymbol{\phi}$ has been discussed from first principles in Appendix A. The exact PDF transport equation from Eq. A.6 is

$$\begin{aligned}\frac{\partial F}{\partial t} + \nabla \cdot \widetilde{\mathbf{u}|\boldsymbol{\psi}} F = &- \frac{\partial}{\partial \psi_\alpha} \left(\left[\frac{1}{\overline{\rho}} \overline{\nabla \cdot \rho D \nabla \phi_\alpha | \boldsymbol{\psi}} + S_\alpha(\boldsymbol{\psi}) \right] F \right) \\ &- \frac{\partial}{\partial \psi_h} \left(\frac{1}{\overline{\rho}} \overline{\left[\frac{Dp}{Dt} + \boldsymbol{\tau} : \mathbf{S} \right] | \boldsymbol{\psi}} \; F \right).\end{aligned} \tag{2.12}$$

In the above equation, derivatives in physical space and time have been written on the left-hand side, whereas derivatives in sample space are on the right-hand side. Further, note that while the reaction source term $\mathbf{S}(\boldsymbol{\phi})$ is in closed form, all conditionally averaged terms need to be modeled. The first of these terms is $\widetilde{\mathbf{u}|\boldsymbol{\psi}}$, and represents velocity-scalar correlations. A gradient diffusion model is used for representing its subfilter component [22, 43, 45, 46] such that

$$\nabla \cdot \widetilde{\mathbf{u}|\boldsymbol{\psi}} F = \nabla \cdot \widetilde{\mathbf{u}} F - \nabla \overline{\rho} D_t \cdot \nabla F / \overline{\rho}, \tag{2.13}$$

where D_t is the turbulent diffusivity.

The first term on the right hand side of Eq. (2.12) is the conditional diffusion term and is further simplified as

$$-\frac{\partial}{\partial \psi_\alpha} \frac{1}{\overline{\rho}} \overline{\nabla \cdot \rho D \nabla \phi_\alpha | \boldsymbol{\psi}} = \nabla \overline{\rho} D \cdot F / \overline{\rho} - \frac{\partial}{\partial \psi_\alpha} \left(\mathcal{M}_F F \right), \tag{2.14}$$

where $\mathcal{M}_F F$ represents the modeled subfilter conditional mixing term. Models for this term are also called micro-mixing models, and have been the focus of research in PDF methods [43, 47–49]. Fox [22] provides a detailed discussion about subfilter mixing, and based on several physical requirements, specifies constraints that the corresponding models need to satisfy. While several micro-mixing models are available, none of the currently available models satisfy all of these constraints. One of the most widely used models for micro-mixing is the interaction by exchange with the mean (IEM) model [42, 43, 50, 51]. In this work, the IEM model will be used for micro-mixing. This model assumes a linear relaxation of the scalar towards its mean value, as follows:

$$\mathcal{M}_F F = \frac{1}{\tau} \left(\psi_\alpha - \widetilde{\phi}_\alpha \right) F. \tag{2.15}$$

Here τ is a mixing time-scale that needs to be specified, and is modeled based on the effective diffusivity and the filter length Δ as [41, 42]

$$\frac{1}{\tau} = C_{mix} \frac{\Delta^2}{D + D_t}, \tag{2.16}$$

where, C_{mix} is a mixing coefficient that needs to be specified.

Finally, the last term in Eq. (2.12) represents correlations between enthalpy, pressure and viscous dissipation. In this work, these correlations are accounted for only in the filtered scales; meaning subfilter correlations between these quantities have been neglected [34–36], leading to the following formulation:

$$\frac{1}{\overline{\rho}} \overline{\frac{Dp}{Dt}} + \boldsymbol{\tau} : \mathbf{S} = \frac{1}{\overline{\rho}} \left(\frac{D\overline{p}}{Dt} + \widetilde{\boldsymbol{\tau}} : \widetilde{\mathbf{S}} \right). \tag{2.17}$$

Note that in low Mach number flows, the pressure derivative as well as the viscous dissipation terms are often negligible, and are dropped from the PDF transport equation [43, 45].

Solution to the PDF transport equation (Eq. 2.12) provides information about the joint-PDF of $\boldsymbol{\phi}$. However, this equation spans $N_s + 5$ dimensions, where N_s is the number of gas-phase species used for representing chemical kinetics. Thus, even for small N_s, the PDF transport equation is high dimensional, and cannot be solved using conventional finite difference or finite volume methods. Instead, specialized approaches that are computationally tractable have to be used, and are discussed next.

2.3.2 Solving the PDF transport equation

For solving the PDF transport equation, both stochastic [42, 44, 45, 51–53] and deterministic approaches [22, 35, 54] have been developed. In the stochastic approach, a notional particle ensemble is evolved in time, physical, and composition spaces to indirectly obtain the solution to the PDF transport equation. The stochastic approach can be further divided into Lagrangian [42, 44, 45, 55] and Eulerian [52, 56] techniques. These methods are coupled to a deterministic LES solver in order to evolve the flow system [41, 44, 57, 58]. This approach has been shown to be highly accurate in several flow configurations [41–44, 50, 59].

The deterministic approach for solving the PDF transport equation is called the direct quadrature method of moments (DQMOM) [22,54,60]. In the fully Eulerian DQMOM approach, the PDF is represented in terms of a finite number of weighted delta function, with each delta function characterized by its weight and location in composition space. Transport equations for these weights and abscissas are then used to obtain the filtered moments of the composition variables as a function of space and time.

These methods for solving the PDF transport equation have been discussed in detail in Chapter 3 and 5. In the next chapter, we use the LES/PDF approach introduced in this chapter for supersonic combustion modeling.

Chapter 3

PDF approach for supersonic combustion modeling

The flow-field inside supersonic combustors is highly compressible with significant interaction between chemical heat release and shock dynamics. The combustion model therefore needs to be robust and well-defined under such extreme conditions. The PDF approach is well suited for this application. However, stochastic PDF methods introduced in Sec. 2.3.2 can lead to significant numerical errors when applied in shock-containing flows [36]. One reason for this is that stochastic algorithms have inherent statistical fluctuations that can couple with shock-induced numerical oscillations leading to numerical instabilities in the LES solver. Also, in confined supersonic flows, the large variations in velocity (zero at the wall to supersonic speeds at the core) could potentially lead to additional issues such as adverse particle number density, which is often corrected by using spatially diffusive procedures [61]. Finally, in any flow, the mixing model introduces another source of numerical diffusion unless specialized algorithms are used to compute the mean concentration in each cell. This aspect is more pronounced when large fluctuations exist in the field variables.

Consequently, for supersonic combustion modeling, the alternative DQMOM approach which is Eulerian and deterministic could be used. While this approach has been used previously in both subsonic [54, 60, 62] and supersonic flows [35], numerical errors associated with practical LES implementation introduce a number of issues. It is shown in this study that in the particular application to non-premixed combustion, the DQMOM transport equations may lead to inconsistent evolution of moments resulting in invalid moment sets.

In this chapter, the DQMOM approach is first discussed in detail. The main sources of numerical errors in DQMOM are then studied. Finally, to improve the numerical accuracy of the quadrate approach, a moment-based alternative called the semi-discrete quadrature method of moments (SeQMOM) is developed.

3.1 Quadrature based moment methods

In quadrature based moment methods, a set of finite number of moments is used to reconstruct the PDF [22]. In general, the PDF is assumed to be composed of component presumed-shapes, which are parameterized using a finite set of variables. Moments of the PDF are then used to obtain these variables. For instance, the PDF could be approximated by a finite set of Dirac delta functions. Each delta function is then characterized by its location in composition space (abscissas) and a height (weight). For compressible flows, the joint-PDF of species mass fraction and sensible enthalpy from Eq. (2.10)

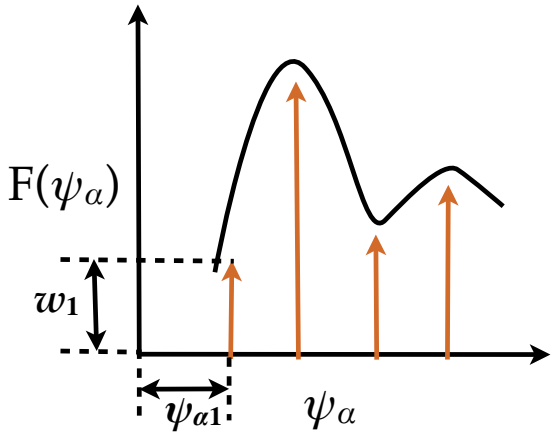

Figure 3.1: Schematic of marginal PDF of ϕ_α approaximated using 4 delta peaks. The weight and abscissa corresponding the the first delta peak have been clearly marked.

can thus be written as

$$F_{\boldsymbol{\phi}}(\boldsymbol{\psi}) = \overline{\rho} \sum_{n=1}^{N_e} w_n \prod_{\alpha=1}^{N_s+1} \delta(\psi_\alpha - \psi_{\alpha n}), \tag{3.1}$$

where, N_e is the number of delta functions used in the approximation. $\psi_{\alpha n}$ and ζ_n are abscissas in the sample space corresponding to the m^{th} specie and enthalpy, and the n^{th} delta function. w_n is the weight corresponding to the n^{th} delta function. To illustrate this, Fig. 3.1 shows the schematic of a marginal PDF of ϕ_α represented using $N_e = 4$. For a system with N_s species, the PDF can thus be specified using N_e weights and $(N_s + 1)N_e$ abscissas.

These weights and abscissas can be obtained in two different ways. In the first approach, moments of the PDF transport equation can be evolved, and the weights/abscissas can be obtained from these moments [63]. In the second approach, transport equations could be obtained directly for the weights and

abscissas [22]. Below, both these techniques are discussed as a prelude to introducing the sources of numerical errors.

3.1.1 Quadrature method of moments (QMOM)

The QMOM approach is widely used for solving population balance equations [63]. Using the definition of the PDF, the unmixed moments of species mass fractions can be defined as

$$\widetilde{\phi_\alpha^j} = \frac{1}{\overline{\rho}} \int_{-\infty}^{\infty} \psi_\alpha^j F(\boldsymbol{\psi}, \zeta) d\boldsymbol{\psi} d\zeta = \sum_{i=1}^{N_e} w_i \psi_{\alpha i}^j, \tag{3.2}$$

where $\widetilde{\phi_\alpha^j}$ represents j^{th} moment of the α^{th} specie. Moments of sensible enthalpy can be similarly defined. In the QMOM approach, transport equations for these moments are solved, which are obtained by appropriately integrating the PDF transport equation (Eq. 2.12).

$$\frac{\partial \widetilde{\phi_\alpha^j}}{\partial t} + \nabla \cdot \widetilde{\mathbf{u}} \widetilde{\phi_\alpha^j} - \frac{1}{\overline{\rho}} \nabla \cdot \overline{\rho}(D + D_t) \nabla \widetilde{\phi_\alpha^j} = \frac{j}{\tau} \left(\widetilde{\phi_\alpha} \widetilde{\phi_\alpha^{j-1}} - \widetilde{\phi_\alpha^j} \right) + j \widetilde{\phi_\alpha^{j-1} S_\alpha(\boldsymbol{\phi})} \tag{3.3}$$

$$\begin{aligned} \frac{\partial \widetilde{\phi_h^j}}{\partial t} + \nabla \cdot \widetilde{\mathbf{u}} \widetilde{\phi_h^j} - \frac{1}{\overline{\rho}} \nabla \cdot \overline{\rho}(D + D_t) \nabla \widetilde{\phi_h^j} = & \frac{j}{\tau} \left(\widetilde{\phi_h} \widetilde{\phi_h^{j-1}} - \widetilde{\phi_h^j} \right) + j \widetilde{\phi_h^{j-1} S_h(\boldsymbol{\phi})} \\ & + j \widetilde{\phi_h^{j-1}} \left(\frac{D\overline{p}}{Dt} + \widetilde{\boldsymbol{\tau}} : \widetilde{\mathbf{S}} \right) \end{aligned} \tag{3.4}$$

Equations (3.3) and (3.4) govern the transport of moments of species mass fraction and sensible enthalpy, respectively. Here $\widetilde{\phi_h^j}$ represents j^{th} moment of sensible enthalpy. The first term on the right hand side in both equations denotes subfilter mixing that is modeled using the IEM model (Eq. 2.15). The

second term on the right hand side arises from the chemical source term, and requires the computation of weights and abscissas for closure. The last term in Eq. (3.4) represents source terms due to pressure gradient and viscous dissipation. For estimating reaction source terms, at every point in space and time, weights and abscissas need to be computed by solving a system of $(N_s + 2)N_e$ nonlinear moment equations obtained from Eq. (3.2). Hence, the QMOM approach requires numerical algorithms that can efficiently solve such a nonlinear system of equations.

This method has been successfully applied to a variety of problems in aerosol modeling that use a univariate particle size distribution [22, 63]. For such problems, the product difference algorithm [63, 64] can be used to calculate weights and abscissas by solving an eigenvalue problem for a matrix of modified integer moments. This method is computationally inexpensive and robust. However, extension of the product-difference algorithm to multivariate PDFs is nontrivial and has not been widely studied. While numerical algorithms for solving this nonlinear problem can be constructed (such as the Newton-Raphson method [65]), such iterative techniques are not robust and are sensitive to initial conditions. Chemical reactions with high scalar production rates tend to change the abscissas significantly between time-steps, making solutions from the previous time-step unsuitable for initialization. As a result, a lack of reliable initial conditions that guarantee convergence prohibit the use of these algorithms in reacting flows.

3.1.2 Direct quadrature method of moments (DQMOM)

The inversion of moments is a significant bottleneck in the use of the QMOM approach. This issue is overcome using the DQMOM technique. The DQMOM approach was developed by Fox [22, 60], and has since been used for solving a variety of problems involving multivariate PDFs [66–68]. Recently, this technique has been extended to the composition-enthalpy PDF transport equation [35, 54, 69]. In this method, transport equations that describe evolution of the quadrature weights and weighted abscissas are solved. These equations are obtained from the transport equation of the composition-enthalpy joint PDF (Eq. 2.12) by substituting the quadrature form of the PDF from Eq. (3.1). This leads to transport equations of the form

$$\frac{\partial \overline{\rho}\mathbf{Y}}{\partial t} + \nabla \cdot \overline{\rho}\widetilde{\mathbf{u}}\mathbf{Y} - \nabla \cdot \overline{\rho}(D + D_t)\nabla \mathbf{Y} = \overline{\rho}\mathbf{B}, \tag{3.5}$$

where $\mathbf{Y}$ is the vector of weights and weighted abscissas and $\mathbf{B}$ represents DQMOM-specific source terms.

$$\mathbf{Y} = \begin{bmatrix} w_n \\ w_n\psi_{\alpha,n} \\ w_n\psi_{h,n} \end{bmatrix}, \mathbf{B} = \begin{bmatrix} a_n \\ b_{\alpha n} \\ c_n \end{bmatrix} \tag{3.6}$$

Source terms a_n, $b_{\alpha,n}$ and c_n need to be computed by matching $(N_s + 2)N_e$ moments of the PDF. Typically a_n is set to zero, which decouples the weights from the evolution of the scalar moments [22, 68]. This permits a simple extension of the method to multivariate problems. The source terms, $b_{\alpha,n}$ and c_n, are computed by matching N_e lower integer moments of the α^{th} scalar and enthalpy respectively [22, 54]. For a two point quadrature representation of

the PDF, $b_{\alpha,n}$ and c_n are given by [22, 54]

$$b_{\alpha,n} =(D + D_t)\frac{w_1\nabla\psi_{\alpha,1}\cdot\nabla\psi_{\alpha,1} + w_2\nabla\psi_{\alpha,2}\cdot\nabla\psi_{\alpha,2}}{2\psi_{\alpha,n} - \sum_k \psi_{\alpha,k}} + w_n\left[\frac{1}{\tau}\left(\widetilde{\phi_\alpha} - \psi_{\alpha,n}\right) + S_\alpha(\boldsymbol{\phi})\right] \tag{3.7}$$

$$c_n =(D + D_t)\frac{w_1\nabla\psi_{h,1}\cdot\nabla\psi_{h,1} + w_2\nabla\psi_{h,2}\cdot\nabla\psi_{h,2}}{2\psi_{h,n} - \sum_k \psi_{h,k}} + w_n\left[\frac{1}{\tau}\left(\widetilde{\phi_h} - \psi_{h,n}\right) + S_h(\boldsymbol{\phi}) + \frac{1}{\overline{\rho}}\left(\frac{D\overline{P}}{Dt} + \widetilde{\boldsymbol{\tau}} : \widetilde{\mathbf{S}}\right)\right] \tag{3.8}$$

By directly solving transport equations for the quadrature weights and weighted abscissas, DQMOM eliminates the need for complex moment inversion algorithms. Also, the Eulerian nature of Eq. (3.6) makes DQMOM significantly computationally less expensive in comparison with stochastic PDF methods [22, 54], and enables easy implementation in standard CFD solvers.

3.2 Numerical errors in DQMOM

While the DQMOM approach overcomes the hurdle of inverting scalar moments to obtain the weights and abscissas, the presence of gradient-type source terms (Eq. (3.7)) is a potential source of numerical errors in LES computations. In this section, these numerical errors are discussed. Note that the numerical errors considered in this work are specific to LES. In the RANS approach, grid convergence is sufficient to remove the errors discussed below. In grid-filtered LES, the inability to assure grid convergence of the solution

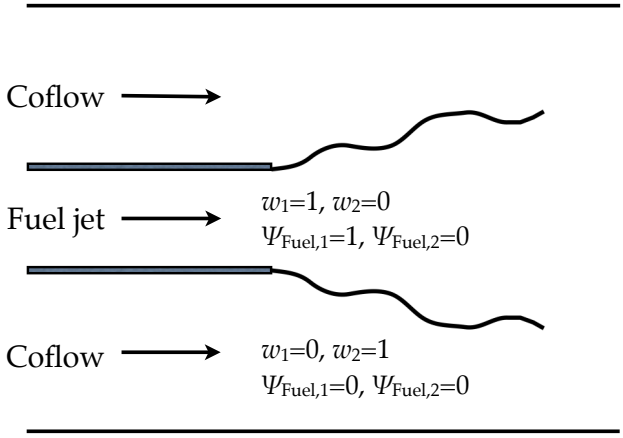

Figure 3.2: Schematic of a fuel jet injected into co-flowing air indicating boundary conditions for weights and abscissas of the fuel specie and the interface between the fuel and oxidizer.

requires that the numerical solutions for a given computational grid incur the least error.

The focus of this work is non-premixed combustion, where two streams with differing species composition enter the computational domain. The composition changes between the streams manifest as differences in weights and abscissas (and consequently moments) at the stream interfaces, leading to steep gradients in regions where mixing is important. Figure 3.2 shows the schematic of a fuel jet injected into co-flowing air. Boundary conditions for weights and abscissas and the interface between the fuel and oxidizer are shown here. Although these sharp changes are associated with both moments as well as the weights and abscissas, these conditions unduly affect the DQMOM equations.

In solving the DQMOM equations, two separate sources of numerical issues can be identified. These are the numerical discretization of the convective and diffusive terms, and the numerical evaluation of the source terms. The latter source of error is primarily due to the inaccurate representation of numerical gradients on a grid that is not sufficiently adequate to support the range of wavenumbers present in an LES computation. All known LES computations rely on the grid-based filtering approach, where the computational mesh acts as an implicit filter since it does not allow any scales smaller than the smallest mesh spacing to be supported. However, numerical errors scale with wavenumber [70, 71], and are highest close to the mesh-scale. Consequently, the near-filter scale features in LES are contaminated by numerical errors [72,73]. Practically, the evaluation of gradient-based quantities is poorly approximated [72, 73]. As a consequence, the gradient-based terms in $b_{\alpha n}$ and c_n are always underpredicted in any discretization scheme, with steeper gradients leading to higher errors. Since the gradient terms provide the dispersion of the abscissas or the generation of subfilter variance, underprediction of this term leads to artificial mixing. Note that the expression for source terms $b_{\alpha n}$ and c_n includes division by distance between the abscissas. As a result, apart from the discretization-based errors, estimation of these source terms leads to additional numerical issues when the abscissas are close to each other. Methods to address these issues have been discussed by Akroyd, *et. al.* [69] and Koo, *et. al.* [35], and the resulting errors arising from these terms in the DQMOM formulation are independent of the errors discussed here.

The discretization-based errors associated with the convective and diffusive operators require more in-depth analysis. Since convective errors are more detrimental due to the nonlinearity of the term, we focus on this aspect here. The issue of numerical errors associated with diffusive operators in the context of scalar moment equations has been studied elsewhere [73]. For the sake of the present discussion, a one-dimensional periodic domain is used. The focus here is the convective transport of scalars, since the numerical solution to the corresponding hyperbolic system is often the source of numerical issues. In this test case, an idealized PDF transport equation is considered.

$$\frac{\partial F}{\partial t} \quad + \nabla \cdot \mathbf{u} F = 0 \tag{3.9}$$

Here F is the PDF of a single conserved scalar. By approximating the PDF using N_e-point quadrature, $2N_e$ transport equations for weights and weighted abscissas that are solved in DQMOM are obtained.

$$\frac{\partial \mathbf{Y}}{\partial t} + \mathbf{u} \cdot \nabla \mathbf{Y} = 0 \tag{3.10}$$

Here, $\mathbf{Y}$ is a vector of weights and weighted abscissas as defined in Eq. (3.6). The corresponding transport equation for moments is obtained from Eq. (3.3).

$$\frac{\partial \mathbf{M}}{\partial t} + \mathbf{u} \cdot \nabla \mathbf{M} = 0 \tag{3.11}$$

Here $\mathbf{M}$ represents a vector of integer moments of the scalar with components $\widetilde{\phi^j}$. An N_e quadrature point DQMOM formulation is expected to accurately reproduce N_e+1 lower integer moments (i.e. $[\widetilde{\phi^0}, \widetilde{\phi^1}, ..., \widetilde{\phi^{N_e}}]$) of the univariate PDF under consideration. For the simple case under consideration, Eq. (3.11)

can be numerically solved. The corresponding solution leads to the method of moments (MOM). If the numerical scheme is conservative, the moments themselves are conserved and lead to a valid moment set.

For studying the effect of the DQMOM formulation on transport of moments, Eq. (3.10) and (3.11) are solved in a periodic one-dimensional domain spanning [0,1]. The convective velocity is assumed to be unity, and is constant throughout the domain. First order numerical schemes are used for spatial and temporal discretization. The time step is computed as $\Delta t = c\Delta x$, where $c = 0.1$. Step conditions are used for initializing weights and abscissas and are shown in Fig. 3.3. Initial conditions for moments are obtained from the weights and abscissas using Eq. (3.2). These step conditions are representative of discontinuities in the scalar field encountered in problems involving non-premixed or partially premixed fuel injection, and are arbitrary enough to be extended to any specific problem.

The hyperbolic nature of Eq. (3.11) leads to a simple analytical solution wherein the initial scalar profile is merely convected in space. In Fig. 3.4, evolution of the second moment computed using MOM and DQMOM is compared with the analytical solution. To evaluate the role of grid size, two cases with grid spacings of 0.01m and 0.001m have been used. Solutions are presented after 0.1 sec, which corresponds to 0.1 flow-through time. It is seen that numerical discretization introduces error in estimating the convection term in both methods. However, the numerical error in MOM reduces as the grid spacing is reduced, and follows the convergence rates (not shown) dictated by

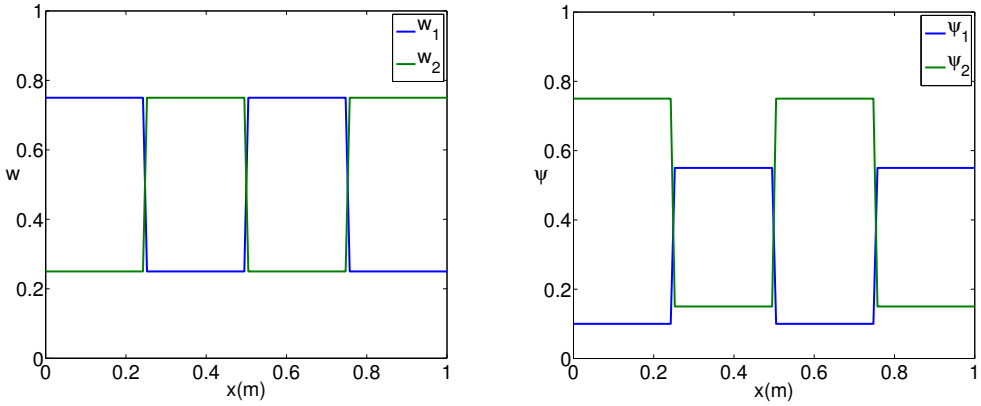

Figure 3.3: Initial conditions for weights and abscissas.

the truncation error. DQMOM, on the other hand, introduces different kinds of numerical errors that do not seem to converge rapidly as dictated by the truncation terms in the Taylor's series expansion.

To understand the differences in the errors from both methods, a detailed analysis of the discretization errors is warranted. Consider

$$\frac{\partial \mathbf{M}}{\partial t} + \mathbf{u} \cdot \nabla \mathbf{M} = \boldsymbol{\varepsilon}_{MOM}, \tag{3.12}$$

where $\boldsymbol{\varepsilon}_{MOM}$ represents numerical error due to finite difference discretization of Eq (3.11) and its magnitude depends on the order of accuracy of the numerical methods used. Similarly, discretization error from Eq. (3.10) is represented by $\boldsymbol{\varepsilon}_Y$. Moment transport equations in DQMOM are constructed from transport equations for weights and weighted abscissas leading to the following relation for the error terms:

$$\boldsymbol{\varepsilon}_{Dq} = \mathbf{J}\ \boldsymbol{\varepsilon}_Y \tag{3.13}$$

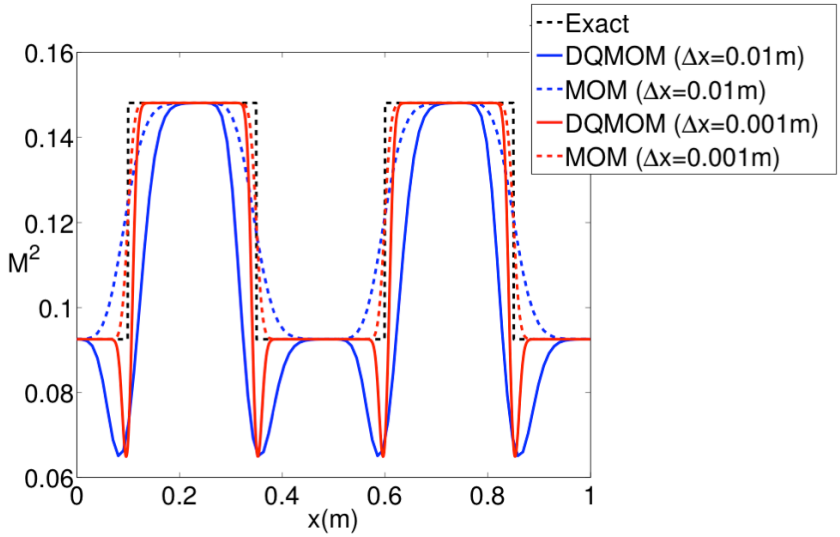

Figure 3.4: Evolution of the second moment in a periodic one dimensional environment. Solution after 0.1 flow-through time computed with mesh sizes of 0.01m (blue) and 0.001m (red) using the method of moments (MOM) (colored dashed lines) and DQMOM (solid lines), and is compared with the analytical solution (dotted black line).

Here $\mathbf{J} = \partial\mathbf{M}/\partial\mathbf{Y}$ is the Jacobian matrix, and $\boldsymbol{\varepsilon}_{Dq}$ represents error in estimating the moments when DQMOM is used. For a two quadrature point DQMOM formulation where $\mathbf{M} = [\widetilde{\phi^0}\ \widetilde{\phi^1}\ \widetilde{\phi^2}]^T$ and $\mathbf{Y} = [w_1\ w_2\ \psi_1\ \psi_2]^T$,

$$\mathbf{J} = \frac{\partial \mathbf{M}}{\partial \mathbf{Y}} = \begin{bmatrix} 1 & 1 & 0 & 0 \\ 0 & 0 & 1 & 1 \\ -\psi_1^2 & -\psi_2^2 & 2\psi_1 & 2\psi_2 \end{bmatrix} \tag{3.14}$$

If the numerical schemes used to solve Eqns. (3.10) and (3.11) have similar truncation errors, it can be expected that the $\boldsymbol{\varepsilon}_Y$ and $\boldsymbol{\varepsilon}_{MOM}$ have similar magnitude. As a result, the constant values in the first two rows of $\mathbf{J}$ imply that the transport equations for the corresponding moments are linearly dependent on transport equations of weights and weighted abscissas, leading to an evolution of these moments that is always consistent with the MOM approach. Evolution of $\widetilde{\phi^2}$ however is a non-linear function of $\boldsymbol{\varepsilon}_Y$ and hence, in general, leads to a solution which is different from the MOM solution. When the scalar fields are smooth, the difference in the evolution of MOM and DQMOM-based moments is not very significant. However, when step-changes in the abscissas are present, these errors are amplified. Consequently, even with first-order finite-difference approximation, a bounded solution for the moments is not obtained with the DQMOM technique. By extending this argument to $Ne > 2$, such nonlinear errors will be present in $\widetilde{\phi^2}$ and higher moments of the PDF. Since these gradients are present at the interface of the fuel and oxidizer, which is the region of utmost interest in terms of scalar mixing and the PDF description, these numerical errors introduce a significant shortcoming of the DQMOM approach.

The main result of this numerical study is that moment transport equations are valid near discontinuities in the field. However, the weight and abscissa equations do not satisfy any conservation rules. Consequently, the errors associated with the discretization of the convection term leads to large errors in the moments predicted by the DQMOM approach. Further, moment transport equations (Eq. 3.3) obtained from the composition PDF transport equation (Eq. 2.12) do not contain gradient-based source terms, and is hence less error-prone in grid-filtered LES [72, 73]. However, inversion of the moments to obtain the weights and abscissas remains a significant hurdle in the use of the MOM approach. Next, a new methodology is proposed that leverages the advantages of both the DQMOM and MOM approaches, and eliminates the disadvantages of these techniques.

3.3 Semi-discrete quadrature method of moments (SeQMOM)

The objective of the SeQMOM approach is to combine the favorable characteristics of moment-based solutions near discontinuities with ease of inversion of moments displayed by the DQMOM approach. As a starting point, the following transformation is considered.

$$d\mathbf{M}(\mathbf{Y}) = \frac{\partial \mathbf{M}}{\partial \mathbf{Y}} d\mathbf{Y}, \tag{3.15}$$

where $\mathbf{Y}$ is the vector of weights and weighted abscissas defined in Eq. (3.6), and $\mathbf{M}$ is a vector of moments of the PDF. In the context of moment transport

equations, Eq. (3.15) can be recast as

$$\frac{\partial \mathbf{Y}}{\partial t} = \mathbf{J}^{-1} \frac{\partial \mathbf{M}}{\partial t}, \tag{3.16}$$

where $\mathbf{J} = \partial \mathbf{M}/\partial \mathbf{Y}$ and $\partial \mathbf{M}_\alpha/\partial t$ is obtained from moment transport equations. $\mathbf{J}$ is analytically computed from Eq. (3.2). Equation (3.16) represents a linear system of equations that is used for evolving weights and weighted abscissas such that they are always consistent with moments. This approach estimates weights and weighted abscissas using discretized moment transport equations, and is therefore called semi-discrete quadrature method of moments (SeQMOM). The only requirement is that $\mathbf{J}$ does not become singular at any location of the domain. As will be explained later (see Sec. 3.4.3), such extraneous conditions can be handled by reverting back to DQMOM locally.

While in theory, $\mathbf{M}$ could contain cross-moments of species, only pure moments are used in this work. The use of IEM model for the micromixing term (see Sec. 2.3) is consistent with this restriction, since the evolution of scalar covariances is not captured by this model. Previous studies using DQMOM [35, 54, 62] have shown that this approach leads to an acceptable agreement with experiments as well as Lagrangian transported PDF methods. The use of unmixed integer moments additionally reduces the numerical complexity involved in solving Eq. (3.16) by decoupling the evolution of weighted abscissas of individual species[1].

[1]Note that a weak coupling still exists via the combustion source term

The N_e integer moments of each species can now be used for computing weighted abscissas of that species using the following formulation:

$$d\mathbf{M}_\alpha(\mathbf{Y};\mathbf{w},\mathbf{Y}_\alpha) = \frac{\partial \mathbf{M}_\alpha}{\partial \mathbf{w}} d\mathbf{w} + \frac{\partial \mathbf{M}_\alpha}{\partial \mathbf{Y}_\alpha} d\mathbf{Y}_\alpha \tag{3.17}$$

Here, $\mathbf{M}_\alpha$ is a vector of N_e unmixed integer moments of the α^{th} specie, $\mathbf{w}$ is a vector of weights, and $\mathbf{Y}_\alpha$ is a vector of weighted abscissas of the α^{th} specie. This leads to

$$\frac{\partial \mathbf{Y}_\alpha}{\partial t} = \mathbf{J}_\alpha^{-1} \left(\frac{\partial \mathbf{M}_\alpha}{\partial t} - \mathbf{J}_{\mathbf{w},\alpha} \frac{\partial \mathbf{w}}{\partial t} \right), \tag{3.18}$$

where, $\mathbf{J}_\alpha = \partial \mathbf{M}_\alpha / \partial \mathbf{Y}_\alpha$ and $\mathbf{J}_{\mathbf{w},\alpha} = \partial \mathbf{M}_\alpha / \partial \mathbf{w}$. An identical equation can be constructed for estimating abscissas of sensible enthalpy. In this formulation, weights need to be separately specified. One way of estimating weights is by constructing a system similar to Eq. (3.16) using moments of the fuel species or a conserved scalar such as mixture fraction [25]. $\mathbf{Y}$ in this case would contain weighted abscissas of fuel species or mixture fraction, and weights $\mathbf{w}$. Weighted abscissas of other species obtained using these weights in Eq. (3.18) would then be conditioned on moments of the fuel species or mixture fraction. This approach, however, can lead to negative conditioned abscissas when fuel species or mixture fraction have low variance, making the solution unphysical. Instead, we solve a separate transport equations for weights, as follows:

$$\frac{\partial \overline{\rho}\mathbf{w}}{\partial t} + \nabla \cdot \overline{\rho}\widetilde{\mathbf{u}}\mathbf{w} - \nabla \cdot \overline{\rho} \left(D + D_t \right) \nabla \mathbf{w} = \mathbf{0}, \tag{3.19}$$

where, $\mathbf{w}$ is a vector of N_e weights. This conserved scalar evolution of weights is identical to that used in DQMOM (Eq. 3.5). The primary advantage of this

approach is that it makes evolution of weights independent of species. While the problem of negativity of abscissas is greatly reduced, non-negativity is still not guaranteed, and will require an additional treatment (see Sec. 3.4.3).

The SeQMOM transport equation (Eq. 3.18) is constructed for the weights and weighted abscissas, which, like DQMOM, eliminates the need for moment inversion algorithms. However, unlike the DQMOM approach, the transport terms in the equation are evaluated using the moments, which was shown to be accurate in the 1-D test case (Sec. 3.2). Further, the use of moments-based evaluation reduces the error induced by the presence of gradient terms in the DQMOM source terms.

Note that numerical problems resulting from the DQMOM formulation have been previously reported in the areas of polydisperse multiphase flows [74–76] and rarefied flows [77, 78]. While the primary focus of these studies was ill-conditioning of DQMOM equations, moment based approaches were introduced to overcome these issues. The resulting conservative moment formulation was nonetheless found to be superior to the DQMOM formulation. However, these methods can best be categorized as variations of QMOM, which will require an inversion algorithm to compute the source terms, and were therefore not applicable in the current context.

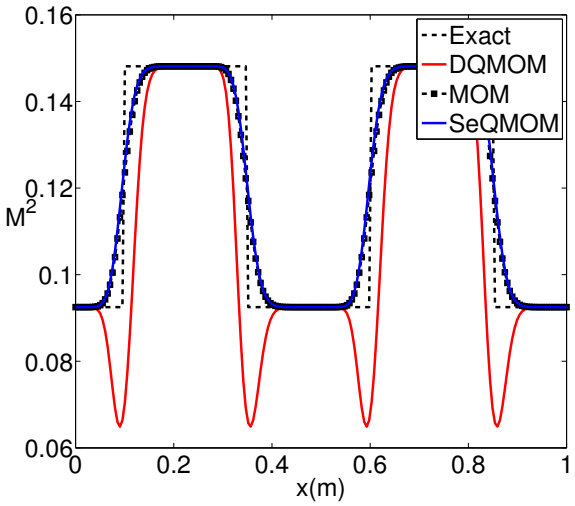

Figure 3.5: Evolution of the second moment of a conserved scalar obtained using various methods after 0.1 flow through time. Note that the solution obtained from SeQMOM is very similar to that obtained from MOM.

3.4 Numerical characteristics of the SeQMOM approach

3.4.1 Accurate estimation of moments

The SeQMOM approach explicitly ensures agreement of estimated abscissas with moment transport equations. This is demonstrated using the numerical example from Sec. 3.2. Figure 3.5 compares the evolution of the second moment of a passive scalar computed using SeQMOM, DQMOM and MOM with the analytical solution after 0.1 flow-through time. The mesh size used here was 0.001 m. It is seen that the moments computed from the abscissas predicted by SeQMOM agree with MOM even in regions of high gradient.

3.4.2 Convergence and order of accuracy

For estimating the order of accuracy, the numerical error in transporting moments using SeQMOM is computed with various numerical schemes and grid sizes. The moment transport is approximated by Eq. (3.11). A two-point approximation is used for representing the quadrature PDF. The initial conditions for the PDF are obtained based on the following conditions for the weights and abscissas:

$$\begin{aligned} w_1 &= 0.5 + 0.4sin(2\pi x), \;\; w_2 = 1 - w_1, \\ \psi_1 &= 0.8 + 0.1sin(2\pi x), \;\; \psi_2 = 0.2 + 0.1sin(2\pi x). \end{aligned} \tag{3.20}$$

These conditions lead to a smooth initial profile for the moments, which ensures minimal numerical dispersion. The domain spans [0,1] and the number of grid points is varied from 25 to 400 cells. A third order Runge-Kutta method is used for integration in time. The L_2 norm of the error for the second moment is computed using the exact solution for this problem. Table 3.1 compares the L_2 norm of error and the corresponding order of convergence obtained by using a first order upwind, second order central, and third order QUICK [79] scheme. The order of error convergence shows that SeQMOM reproduces the order of accuracy expected from these numerical schemes. This study shows that SeQMOM can be used with higher order numerical techniques employed in LES without any change in the accuracy of the underlying scheme. However, to ensure realizability, additional issues discussed in Sec. 3.4.3 have to

Table 3.1: L_2 error for the second moment computed using SeQMOM.

	Grid size	L_2 error	L_2 order
First order upwind	25	$18.7\text{x}10^{-10}$	-
	100	$4.5\text{x}10^{-10}$	1.01
	400	$1.1\text{x}10^{-10}$	1.003
Second order central	25	$15.6\text{x}10^{-11}$	-
	100	$0.95\text{x}10^{-11}$	2.006
	400	$0.06\text{x}10^{-11}$	2.002
Third order QUICK	25	$28.9\text{x}10^{-12}$	-
	100	$0.44\text{x}10^{-12}$	3.0
	400	$0.01\text{x}10^{-12}$	3.0

be considered.

3.4.3 Robustness of the approach

Although the SeQMOM approach accurately reproduces moments of the PDF, the differential-algebraic nature of Eq. (3.18) precludes its direct implementation in complex numerical simulations. The first problem is encountered due to ill-conditioning of the SeQMOM equations (Eq. (3.18)). These equations are well-defined as long the Jacobian matrix, $\mathbf{J}_\alpha$, is not singular. If the delta peaks are too close to each other, then this matrix will approach the singularity condition, making it impossible to estimate the abscissas. The second problem is related to the physical bounds for abscissas of the PDF. For the composition-enthalpy joint-PDF, any method must ensure positivity and boundedness of not only the moments, but also the abscissas of the PDF. For instance, abscissas of composition variables should be between

0 and 1. One source of unphysical abscissas is dispersion errors resulting from the use of higher order numerical schemes for transporting moment vectors in the presence of discontinuities [80]. In general, the SeQMOM approach does not guarantee that abscissas estimated from the moments would be within any physical bounds.

Note that the problem of ill-conditioned equations occurs in the DQMOM approach also. Here, the source terms for the abscissas will become singular (Eq. (3.7), (3.8)) under similar conditions as well. This problem however, can be addressed by suitably restricting these source terms when abscissas are close to each other [35,69]. Also, DQMOM has a transport equation based evolution of weighted abscissas. By using total variation [81] or scalar bounded [79] schemes, it is possible to ensure positivity. Based on these observations, a hybrid SeQMOM-DQMOM approach is proposed as a practical alternative to ensure robustness. The DQMOM-based estimation of the PDF can thus be used in spatial locations where SeQMOM is not applicable. Here, the DQMOM transport equations (Eq. 3.5) are evolved simultaneously along with the SeQMOM equations. While this increases the computational cost, it also ensures robustness. Compared to stochastic approaches, this hybrid method is still significantly cost-effective.

The use of the DQMOM solution in some parts of the domain will invariably reduce the accuracy associated with the SeQMOM approach. However, it should be noted that the DQMOM and SeQMOM equations evolve identically in regions that do not have steep gradients. The problem of ill-

conditioning occurs only when the abscissas collapse in composition space, which occurs in regions where the mixing is complete. In these regions, the shape of the sub-filter PDF is simple, and the use of the DQMOM approach will not introduce significant errors.

The realizability error resulting from scalar discretization schemes is difficult to handle. It is possible to use bounded non-linear discretization schemes [81, 82] that will guarantee that the DQMOM solution stays within the scalar bounds. While this will ensure that the moments stay positive, it is still possible that the moment set is unrealizable. Alternately, moment correction [80] or realizable schemes for moments [83] could be used. For the test cases discussed here, bounded scalar schemes were found to be sufficient to guarantee realizable moment sets in regions of interest.

Finally, in the hybrid formulation, the solution switches between SeQMOM and DQMOM based on the criterion discussed in this section. This switch primarily represents how the source terms are evaluated, thereby implying only a change in the composition-space evolution rate. Consequently, this procedure has minimal impact on the evolution equations in terms of numerical stability. The impact of the hybrid formulation on accuracy is further evaluated in greater detail using a numerical example in Sec. 4.2.

3.5 Summary

The quadrature based approach for solving population balance equations was presented in this chapter, with specific emphasis on DQMOM. Nu-

merical errors in DQMOM severly restrict its accuracy, and therefore an alternative SeQMOM approach was developed using a conservative moment-based formulation. Key numerical properties of this new method were then discussed. In the next chapter, computational studies using SeQMOM are presented for flows of engineering interest.

Chapter 4

LES-based studies using SeQMOM

In this chapter, the numerical implementation of SeQMOM in a practical LES solver is first discussed. This is followed by an inert planet jet simulation where the ability of the new approach towards representing higher moments of the PDF is evaluated. A supersonic reacting jet and a cavity stabilized combustor are then studied using the LES/SeQMOM approach.

4.1 LES-based numerical implementation

The SeQMOM equations are implemented in a high Mach number LES solver developed in-house [84,85]. For shock capturing, a 5th order WENO [81] scheme is used for computing convective fluxes in the continuity and momentum equations. A dynamic Smagorinsky model [33] is used for closing the subfilter stress term in the momentum equation. Enthalpy and scalar fluxes are computed using a third order QUICK [79] scheme. An MPI-based parallel implementation allows efficient computation of large problems. Further details of the flow solver can be obtained elsewhere [84–86].

In the hybrid SeQMOM-DQMOM approach, $N_e(2N_s + 3)$ transport equations need to be evolved. This includes N_e equations for weights based

on Eq. (3.19), $N_e(N_s+1)$ equations for moments using SeQMOM based on Eq. (3.3) and (3.4), and $N_e(N_s+1)$ equations for DQMOM weighted abscissas based on Eq. (3.5). Filtered values of the reaction source terms $\widetilde{\phi_\alpha^{j-1}S_\alpha(\boldsymbol{\phi})}$ and $\widetilde{\phi_h^{j-1}S_h(\boldsymbol{\phi})}$ in the moment transport equations are estimated from knowledge of the weights and abscissas of the joint-PDF. For instance,

$$\widetilde{M_\alpha^{j-1}S_\alpha}(\mathbf{Y}) = \sum_{i=1}^{N_e} w_i \psi_{\alpha,i}^{j-1} S_\alpha(\boldsymbol{\psi}_i, \zeta_i), \tag{4.1}$$

where, $[\boldsymbol{\psi}_i, \zeta_i]$ is the composition-enthalpy vector for the i^{th} quadrature point. In Eq. (3.18), Jacobian matrices $\mathbf{J}_\alpha$ and $\mathbf{J}_{\mathbf{w},\alpha}$ are analytically evaluated so that the solution to the corresponding differential-algebraic system of equations is greatly simplified. For instance, for $N_e = 2$, these matrices have the following form:

$$\mathbf{J}_\alpha = \begin{bmatrix} 1 & 1 \\ 2\psi_{\alpha,1} & 2\psi_{\alpha,2} \end{bmatrix}, \mathbf{J}_{\mathbf{w},\alpha} = \begin{bmatrix} 0 & 0 \\ -\psi_{\alpha,1}^2 & -\psi_{\alpha,2}^2 \end{bmatrix} \tag{4.2}$$

$\mathbf{J}_h$ and $\mathbf{J}_{\mathbf{w},h}$ have a similar form. Here, note that $|\mathbf{J}_\alpha| \propto (\psi_{\alpha,2} - \psi_{\alpha,1})$. Hence, for avoiding the problem of ill-conditioning discussed in Sec. 3.4.3, DQMOM-based abscissas are used in grid cells where the distance between the abscissas is smaller than 5% of the mean value. In all other cells, the SeQMOM-based abscissas are estimated and checked for their respective physical bounds. In locations where their values are unphysical, DQMOM-based abscissas are used, and moment fields are re-evaluated using the updated abscissas. For convenience, the hybrid SeQMOM-DQMOM approach is henceforth referred to as simply the SeQMOM approach.

The boundary conditions for the PDF are based on values of the centered moments. Typically, this includes specification of mean species mass fractions and enthalpy, with variance set to zero. For instance, the fuel mass fraction $\widetilde{\phi}_{fuel}$ is set to 1, while the variance $\widetilde{\phi''^2}_{fuel}$ is set to zero at the fuel inlet. In the context of quadrature based methods, two approaches have been previously used for specifying the boundary conditions [35, 54, 69]. With a two-point quadrature representation of the PDF, the boundary conditions for weights and abscissas can be specified as: (a) $\mathbf{w} = [1, 0]$, $\psi_{fuel} = [1, 0]$, or (b) $\mathbf{w} = [t, 1-t]$, $\psi_{fuel} = [1, 1]$, where $0 < t < 1$. Note that both DQMOM as well as SeQMOM solve transport equations for weighted abscissas. Therefore, as noted by Koo, *et. al.* [35], estimation of abscissas can encounter numerical singularities when one or more weights are close to zero. In this context, method (b) is desirable since the singularity condition for weights is avoided. Another advantage with method (b) is that boundary conditions for higher N_e are straightforward. In this work, method (b) is used for specifying the boundary conditions.

When implemented with detailed chemistry mechanisms, SeQMOM requires numerical integration of the chemistry source term using a stiff ordinary differential equation (ODE) solver. In each computational cell, the number of calls to the ODE solver is equal to the number of quadrature points used for representing the PDF. Typically, the ODE integration step incurs the largest computational cost. In this work, an MPI-based algorithm was developed that significantly reduced the computational cost. The algorithm utilizes the fact

that only a small fraction of the computational domain has conditions suitable for combustion. Consequently, when a large number of processors are used for computations, only a handful of processors end up using ODE integration, thereby adversely affecting parallel efficiency. Keeping this in mind, first, cells that require ODE integration are identified based on composition and enthalpy variables for a given quadrature point. One way of doing this is by roughly estimating the chemistry time scale based on reaction source terms, and then comparing it with the solver time-step. Next, integration of ODEs is equally divided between all processors. For instance, if x cells require ODE integration, each processor is assigned x/N_{proc} ODE problems, where N_{proc} is the total number of processors used. This load-balancing greatly increases parallel efficiency. For example, the use of this algorithm in the study in Sec. 4.4 reduced total computational time by a factor of 3.

4.2 Non-reacting compressible jet

In this study, the SeQMOM approach is used for studying the evolution of a conserved scalar in a non-reacting planar jet. The flow configuration consists of a central fuel jet with two co-flowing streams on either side. A two delta-peak ($N_e = 2$) representation is used for representing the PDF. For comparative evaluation, scalar evolution is simultaneously tracked using method of moments (MOM) and DQMOM. For $N_e = 2$, an equivalent MOM computation requires solution to the first two integer moments of the fuel fraction. Boundary conditions for the jet and co-flow streams are given in

Table 4.1: Boundary conditions for the planar jet.

	Jet	Co-flow
w_1	0.6	0.4
w_2	0.4	0.6
ψ_{11}	1	0
ψ_{12}	1	0
Mach No.	0.5	0.8
Temperature (K)	300	250
Density(kg/m^3)	1.41	1.0

Table 4.1. Time-varying turbulent inflow obtained from a separate channel simulation was used for specifying velocity, density and temperature at the jet inlet. Uniform values were used for specifying conditions at the co-flow inlet. Initial conditions for the flow variables as well as weights and abscissas were based on the co-flow boundary conditions. The IEM mixing model used in this study requires specification of the mixing constant C_{mix} (see Eq. 2.16). In this study, $C_{mix} = 2$ is used without any loss of generality. The computation domain spanned $45h \times 12h \times 3h$ in the streamwise, crosswise and spanwise directions, respectively, where $h = 20mm$ is the jet height. A computational mesh spanning $768 \times 150 \times 50$ points was used. To evolve one flow-through time based on jet velocity, roughly 4 hours of computation was required on 64 processors. The relative computational effort spent on MOM, DQMOM and SeQMOM is roughly $1 : 2 : 4$.

Figure 4.1 shows time averaged contours of scalar mass fraction. Note that the mean mass fraction estimated by all of these methods is identical.

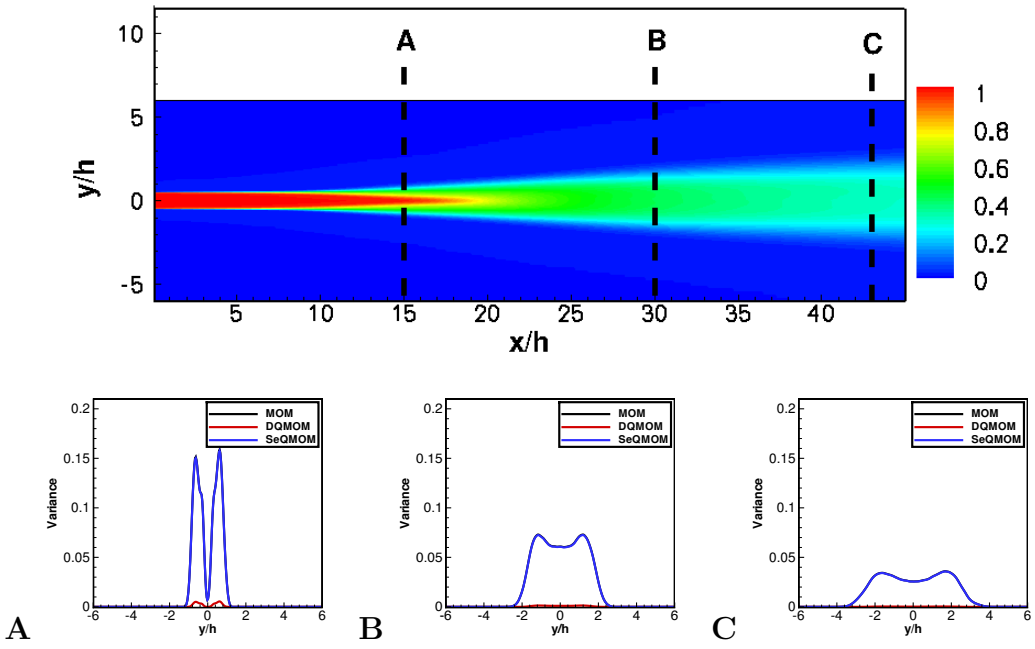

Figure 4.1: Time averaged contours of mixture fraction (top). Variance of mixture fraction obtained using various methods (bottom) is compared at (A) x/h=15, (B) x/h=30, and (C) x/h=43. Note that the variance prediction using SeQMOM is very similar to that obtained from MOM.

Figure 4.1 further compares the subfilter scalar variance estimated using various methods at three spatial locations. Variance is produced due to gradients in the scalar field at the jet periphery, and its magnitude reduces due to mixing as the flow evolves in the downstream direction. At each of the spatial locations indicated, the variance estimate by DQMOM is significantly lower than both MOM and SeQMOM. In general, there is very little difference between the MOM and SeQMOM errors. To further quantify the difference between the solution estimated by SeQMOM and DQMOM, deviation of the corresponding solutions from MOM is analyzed. Figure 4.2 compares the normalized L2-norm of the error from DQMOM and SeQMOM methods. The L2-norm has been normalized by the local value of the MOM scalar variance. In the first few cells ($x/h \sim 1$) the error in DQMOM is identical to SeQMOM. This is the region where the hybrid SeQMOM method selects the DQMOM abscissas due to ill-conditioning. As variance is produced, the problem of ill-conditioning reduces. Some cells however still select DQMOM based on the positivity criterion. Finally, after $x/h \sim 10$, the near-constant value of the error indicates that the hybrid method always selects the SeQMOM solution, leading to a solution very similar to MOM. DQMOM, on the other hand, vastly under predicts variance. This is because numerical dissipation resulting from estimation of the source terms and errors associated with the diffusion term add up with the errors associated with convection discussed in Sec. 3.2. In spite of employing the hybrid methodology, the SeQMOM approach still produces a much lower error compared to the DQMOM method.

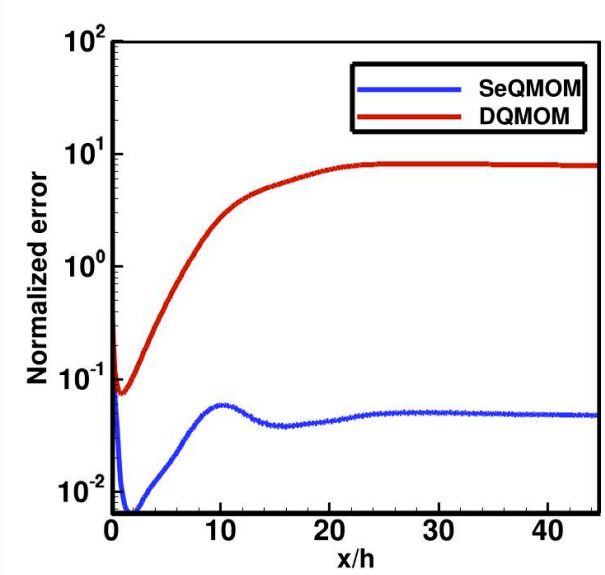

Figure 4.2: Normalized L_2-norm of error. Error here is defined relative to the method of moments (MOM) solution.

4.3 Supersonic reacting jet

The second study involves a supersonic hydrogen jet, and is primarily used for demonstrating the SeQMOM approach in cylindrical coordinates. This simulation is based on the experimental study of Evans et al. [87]. A schematic of the experimental configuration is shown in figure 4.3. In the experiment, hydrogen is injected at Mach 2 with a stagnation temperature of 450K. The co-flow consists of air vitiated using a hydrogen combustor. The resulting test gas has a Mach number of 1.9 and total temperature of 2250K.

The computational domain starts from the plane in which hydrogen is injected, and spans 30D x 5.5D in the stream-wise and radial directions

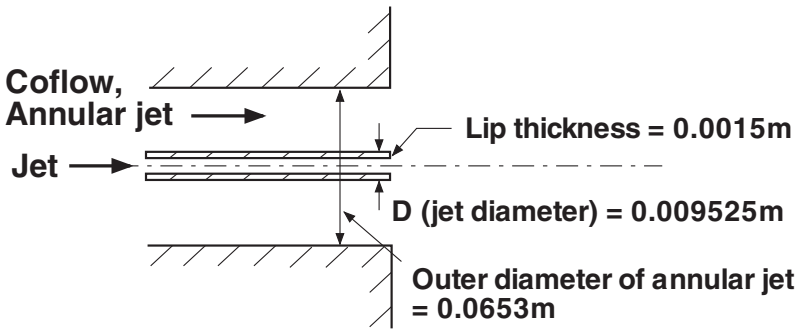

Figure 4.3: Schematic of the supersonic hydrogen jet experiment.

Table 4.2: Boundary conditions for the flow variables.

	Jet	Co-flow
Mach No.	2.0	1.9
Temperature (K)	250	1495
Density(kg/m^3)	0.097	0.2
w_1	0.6	0.4
w_2	0.4	0.6
$\psi_{H_2,1}$	1.0	0
$\psi_{H_2,2}$	1.0	0
$\psi_{O_2,1}$	0	0.241
$\psi_{O_2,2}$	0	0.241
$\psi_{H_2O,1}$	0	0.281
$\psi_{H_2O,2}$	0	0.281

respectively. The mesh consists of $512 \times 96 \times 32$ points in the stream-wise, radial and circumferential directions respectively. Turbulent inflow conditions are required for ensuring proper mixing of the jet. In this case, time dependent inflow profiles obtained from a separate pipe simulation are used for the jet. Inflow conditions for the coflow are based on mean turbulent boundary layer correlations. A two delta-peak formulation was used for representing the PDF. Hydrogen-air chemical kinetics are represented using a detailed 9 species and 19 steps mechanism [88]. Boundary conditions for flow variables as well as weights and abscissas of major species have been listed in Table 4.2. The mixing constant C_{mix} for the IEM micro-mixing model (see Eq. 2.16) is set as 5.

Figure 4.4 shows instantaneous contours of OH mass fraction and temperature. The hydrogen jet interacts with the vitiated co-flow and reacts instantly. The thick cylinder wall assists in turbulent mixing and reactions, and peak temperature is observed in the corresponding separation region in the vicinity of this wall. Complete mixing is however not achieved within the domain considered. OH contours further indicate that reactions are limited to the thin shear layer between the jet and the co-flow. In Fig. 4.5, total pressure predicted by the simulation is compared with experimental results. While the pressure change predicted by the simulation agrees well with the experiment, the pressure near the mixing layer as well as the jet center is lower in the simulation. These differences can be attributed to uncertainties in experimental measurements as well as inflow conditions.

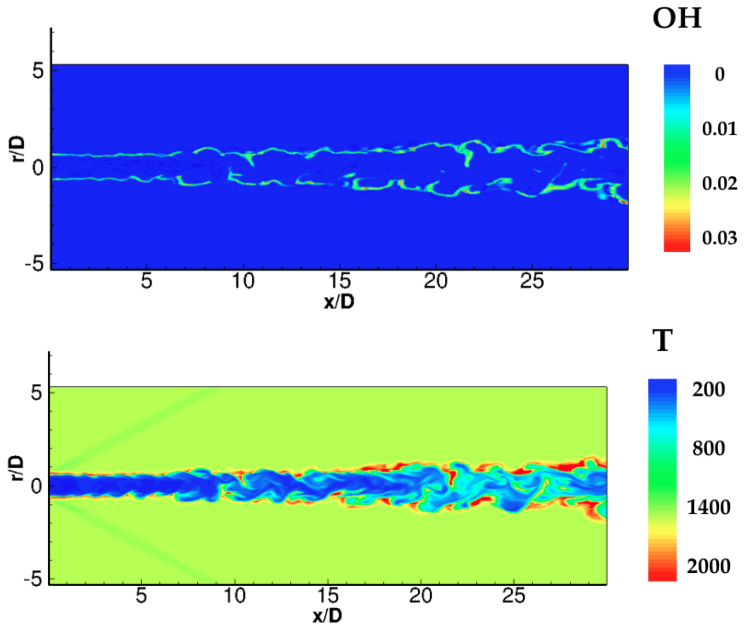

Figure 4.4: Instantaneous contours of OH mass fraction and temperature for the supersonic hydrogen jet.

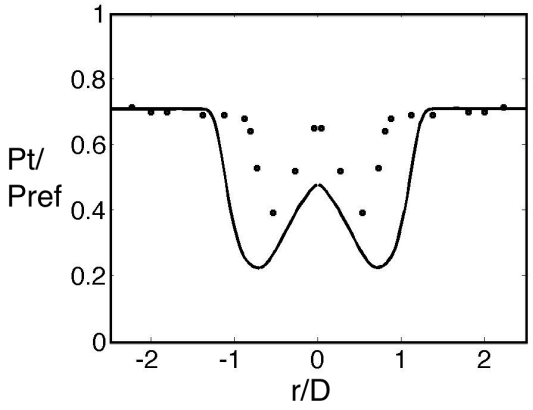

Figure 4.5: Total pressure computed at $x/D = 13.8$ compared with experimental results of Evans, et al. [87]. Simulation: (—), Experiment: (•)

4.4 Supersonic cavity stabilized combustor

The purpose of this simulation is to demonstrate the applicability of SeQMOM in a realistic combustor configuration. The test case under consideration is based on the supersonic cavity-stabilized flame experiment of Micka and Driscoll [11]. This configuration was previously studied by Koo, *et. al.* [35] using the DQMOM approach. Figure 4.6 provides a schematic of the flow configuration. The incoming air stream has a Mach number of 2.2 and a total temperature of 1490K. A sonic hydrogen jet issues from the bottom wall at a distance $3.5h$ upstream of the cavity leading edge. The gas phase chemistry is represented using a detailed hydrogen-air reaction mechanism [88] consisting of 9 species and 19 steps. A joint-PDF of 8 species and enthalpy is evolved, and continuity is used for computing abscissas of the ninth species. Boundary conditions for the PDF are specified such that the mean corresponds to the prescribed experimental conditions, while the variance is set to zero. Walls are assumed to be adiabatic. Detailed boundary conditions are listed in table 4.3. Turbulent inflow for the isolator was obtained from a separate boundary layer simulation. Initial conditions for the flow variables as well as weights and abscissas were based on the freestream boundary conditions. The IEM mixing constant $C_\phi = 5$ in this study. A multiblock structured grid with $350 \times 100 \times 50$ points in the main flow pathway and $100 \times 50 \times 50$ points in the cavity is used for this simulation. One flow-through time based on freestream velocity required roughly 4 hrs of computations on 128 processors.

In this study, a two point quadrature formulation ($N_e = 2$) has been

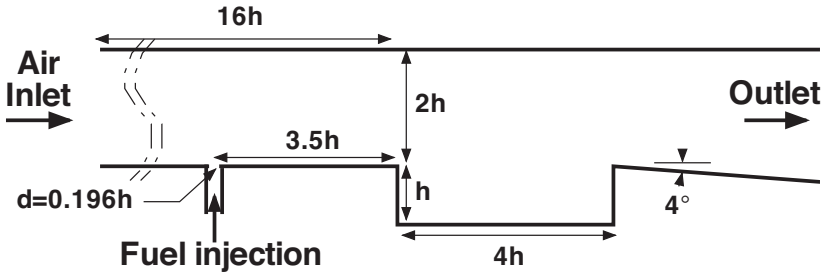

Figure 4.6: Schematic of the cavity-stabilized combustor.

Table 4.3: Boundary conditions for the supersonic cavity based combustor.

	Isolator	H_2 jet
Mach No.	2.2	1
Temperature (K)	710	240
Density(kg/m^3)	0.27	0.4
w_1	0.2	0.8
w_2	0.8	0.2
$\psi_{O_2 1}$	0.233	0
$\psi_{O_2 2}$	0.233	0
$\psi_{H_2 1}$	0	1
$\psi_{H_2 2}$	0	1

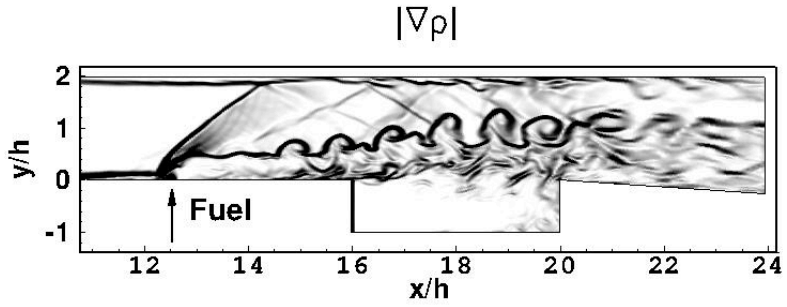

Figure 4.7: Instantaneous contour of the magnitude of density gradient plotted along the central plane.

used. While using higher order quadrature theoretically increases accuracy of the quadrature formulation through better representation of higher order statistics, in this cavity-stabilized combustor configuration, higher order statistics did not play a decisive role in flame stabilization (as discussed below). Consequently, increasing the number of quadrature points in this simulation was not expected to noticeably improve accuracy.

Figure 4.7 shows instantaneous contours of the magnitude of density gradient $|\nabla\overline{\rho}|$. Injection of hydrogen leads to a jet in supersonic crossflow configuration. The flow field is characterized by a strong shock upstream of the fuel jet that causes boundary layer separation. Fuel diffuses upstream of the jet into the recirculation zone resulting from separation. Shock waves reflected from the top wall interact with the fuel jet and influence the jet trajectory. Large density fluctuations are observed in jet wake and the cavity shear-layer leading to strong shock-turbulence-chemistry interactions.

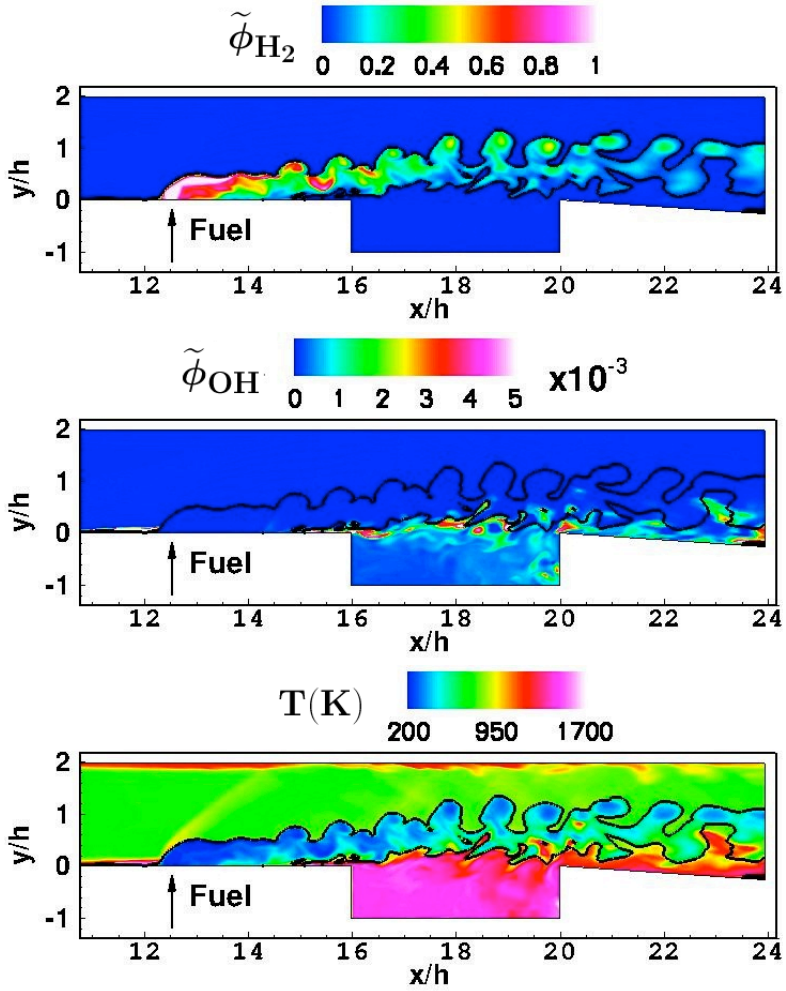

Figure 4.8: Instantaneous contours of H_2 and OH mass fraction, and temperature plotted along the central plane. The iso-value of stoichiometric mixture fraction is indicated by a solid line.

In this configuration, fuel entrains the cavity from the downstream side. Recirculating flow inside the cavity leads to conditions favorable for combustion, thereby enabling oxidation of the fuel. High temperature gases then exit the cavity from the upstream side. This further enhances reactivity in the wake of the fuel jet. The cavity thus acts like a high temperature heat source and sustains reactions in the combustor. Figure 4.8 shows the instantaneous contours of H_2 and OH mass fractions, and temperature along the central plane. The hydroxyl radical is present in the cavity as well as in the jet wake, indicating stable combustion in these regions. The recirculation upstream of the jet also provides conditions favorable for reactions, as indicated by high OH concentration in this region. Overall, reactions are observed at lean stoichiometric conditions, and the intermittency in OH concentrations indicates local extinction.

For comparative evaluation, two additional simulations were performed. One used a DQMOM based combustion model, and the second used a laminar chemistry assumption for estimating the combustion source term. In the latter case, it is assumed that the scalars are fully mixed at the sub-filter scale, and the chemical source terms are directly computed using the filtered scalar values. The laminar chemistry assumption can be interpreted as a quadrature method with single-point ($N_e = 1$) representation of the PDF. Also, in addition to species mass fractions and enthalpy, both SeQMOM and DQMOM simulations included an additional mixture fraction variable. Figure 4.9 shows the time-averaged contours of mixture fraction variance estimated using SeQ-

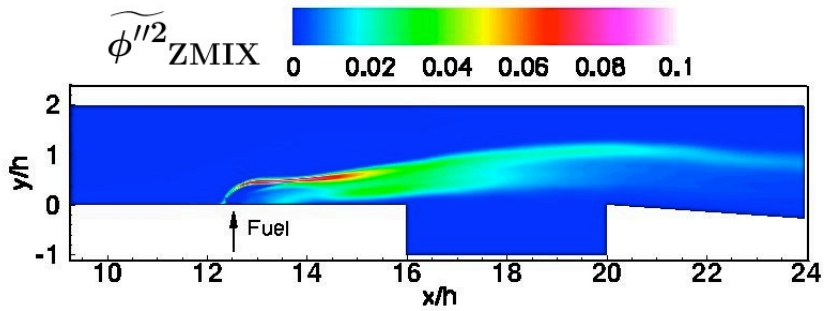

A: SeQMOM

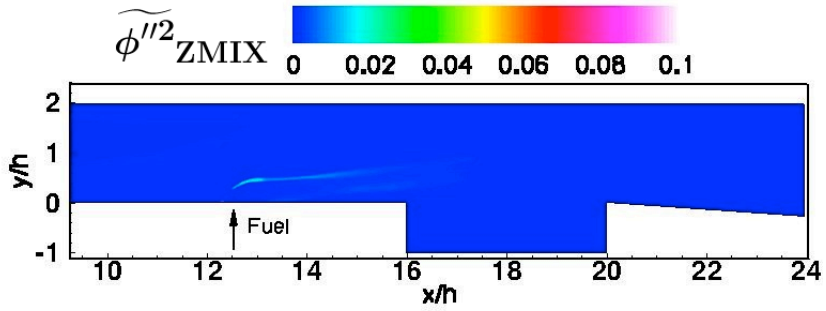

B: DQMOM

Figure 4.9: Time averaged contour of subfilter variance of mixture fraction estimated by (A) SeQMOM and (B) DQMOM plotted along the central plane.

MOM and DQMOM. As also seen in Sec. 4.2, numerical error in DQMOM leads to severe underprediction of variance. In general, such underprediction is associated with faster subfilter mixing. In regions of high temperature, this could lead to increased reactions, while increased mixing could also lead to extinction in certain cases.

In the experiment [11], images of flame luminosity indicated that flame stabilization was achieved in the wake of the fuel jet and the cavity. The corresponding information for the simulations is provided by time averaged contours of OH mass fraction. Figure 4.10 shows that the laminar chemistry simulation reports significantly higher reaction rates in comparison with both SeQMOM and DQMOM. High OH concentration in the boundary layer behind the fuel jet indicates that flame stabilization in this case is caused by the recirculation zone upstream of the jet, which is contrary to what has been reported in the experiment. This highlights the important role played by subfilter scalar correlations in predicting reactions. The reaction zone structure predicted by both SeQMOM and DQMOM is identical, and is consistent with the experiment. For highlighting the difference between reaction rates predicted by the two methods, the difference between OH predictions by the two methods is shown in Fig. 4.11. The OH prediction by DQMOM in the jet wake is lower than the prediction from SeQMOM by a factor of two, and as seen in Fig. 4.9, primarily results from under prediction of variance by DQMOM in this region. Artificial sub-filter mixing caused by numerical diffusion leads to extinction in the DQMOM solutions in this region. Nonetheless, in

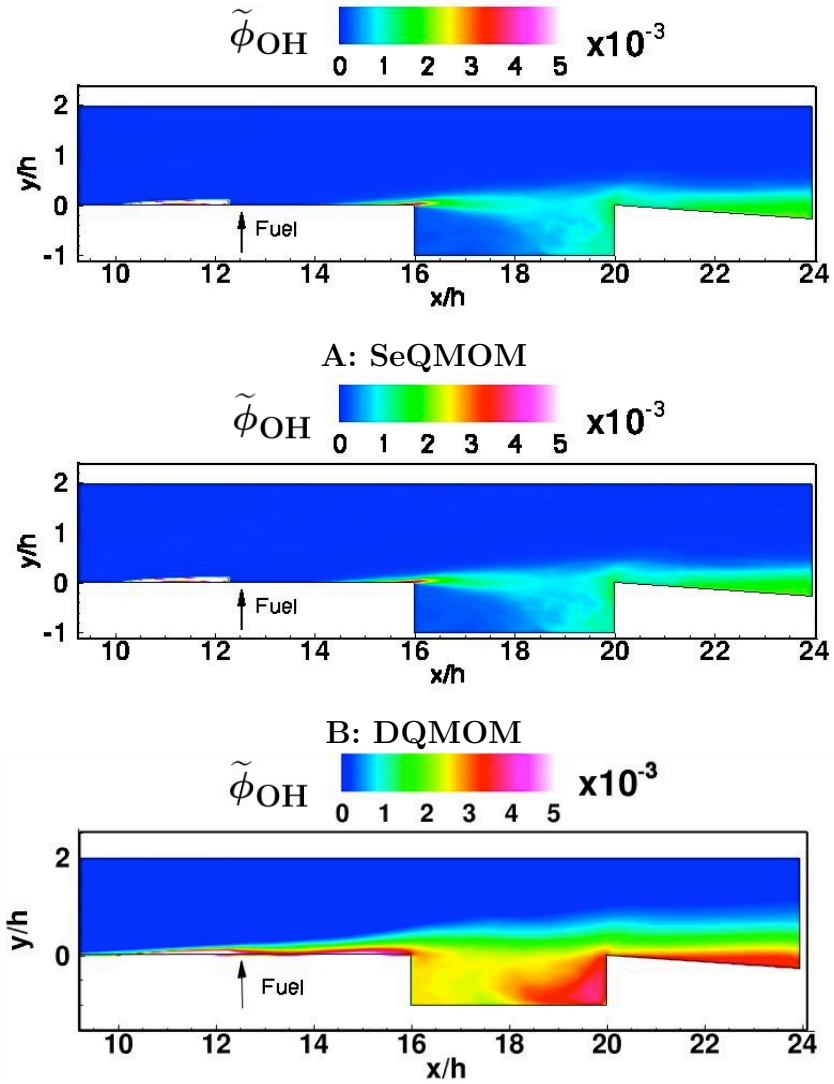

Figure 4.10: Time averaged contours OH mass fraction using (A) SeQMOM, (B) DQMOM and (C) Laminar chemistry plotted along the central plane.

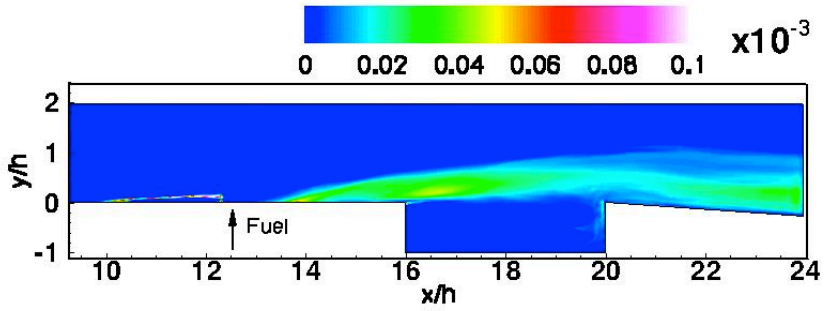

Figure 4.11: Difference between OH mass fractions predicted by SeQMOM and DQMOM ($(\widetilde{\phi}_{OH})_{SeQMOM} - (\widetilde{\phi}_{OH})_{DQMOM}$) plotted along the central plane.

the cavity where the fluid is well-mixed, the predictions from both methods are identical. These results indicate that the DQMOM method, in spite of its numerical errors, predicts first-order statistics qualitatively accurately. However, higher-order statistics such as subfilter variance are better captured by the SeQMOM method. Consequently, flow systems where higher order statistics are critical for the evolution of the flame structure will be better captured by the SeQMOM approach.

4.5 Conclusions

In this study, a new quadrature based method called the SeQMOM approach was developed and validated for LES-based simulation of turbulent combustion. The simulation of non-premixed flames introduces sharp gradients in scalar fields that lead to increased numerical errors in conventional quadrature methods. By recognizing that the best numerical strategy is to

ensure that the moments of the PDF are evolved consistently, the SeQMOM approach is formulated. Numerical tests in 1D as well as 2D non-reacting flow configurations show that the new method reproduces the moments-based solution very closely, thereby increasing the consistency of the approach. To ensure robustness, the SeQMOM approach is solved simultaneously with the DQMOM method, with the DQMOM solution used to reconstruct the PDF in regions where the abscissas of the PDF are very close in composition space. A realistic supersonic combustor is used to demonstrate the applicability of the SeQMOM approach in practical flow configurations. Here again, the DQMOM approach vastly underpredicts subfilter scalar variances, indicating artificial mixing. The computational cost of using the SeQMOM is nearly twice that of the DQMOM approach, but is an order of magnitude less expensive compared to conventional stochastic Monte-Carlo approaches.

Chapter 5

Soot modeling in turbulent flames

In this chapter, we focus on the second problem of interest, namely modeling soot formation in turbulent flames. As discussed in Sec. 1.2, soot formation is an extremely intermittent process. Consequently, the LES approach is well suited for studying soot formation, as unsteady features in large energy-containing scales are explicitly resolved. Nonetheless, the small-scale correlations between gas-phase scalars and soot precursors need to be described. Such correlations are highly nonlinear, and have to be modeled. Typically, the soot population is described using a set of moments of the underlying number density function (NDF). In this context, small-scale correlations are best represented by a one-point one-time joint PDF of the gas-phase scalars and soot moments.

Due to the inherent challenges in describing soot precursor chemistry, turbulence, and combustion processes, not much attention has been given to the modeling of this joint-PDF. In LES, the subfilter correlations between soot and the gas-phase composition are often neglected. In this case, the PDF is written as the product of the marginal PDFs of gas phase scalars and soot moments. However, given the high sensitivity of soot to the flame

characteristics, this approximation could potentially introduce large errors. Recently, Mueller and Pitsch [89] have developed a presumed PDF approach, in which the independence of these variables is assumed, but the marginal PDFs of the soot moments are modeled using an intermittency related term. In the Reynolds-averaged Navier Stokes (RANS) formulation, Lindstedt *et. al.* [90] have directly solved the joint-PDF using a high-dimensional transport equation. It was found that accounting for the composition-soot correlations resulted in significant changes in the soot profiles. Chandy *et. al.* [91] have used the PDF approach in the context of LES, but with a simplified model for the soot chemistry.

In this work, the focus is to combine the PDF approach with a detailed description of unsteady soot precursor chemistry, particulate dynamics, and gas-phase radiation. Detailed chemistry for soot precursor evolution and the gas-phase turbulent combustion process is described using a modified flamelet/progress variable approach. To account for radiation effects, an additional state space parameter in the form of the radiation heat loss parameter is used. The soot population is described using a bivariate volume/surface area formulation that allows for surface processes to be modeled more accurately. Finally, the joint-PDF of the soot moments and the gas-phase scalars is formulated in cylindrical coordinates, and is solved using a Lagrangian Monte Carlo technique.

5.1 Gas-phase chemistry

Gas-phase precursors to soot formation are large aromatic compounds called polycyclic aromatic hydrocarbons (PAH) [92–95]. Extremely large chemistry mechanisms are necessary for taking into account PAH formation pathways [37, 92, 96]. Consequently, for computational tractability, flamelet generated manifolds wherein only a few scalar are used for representing the gas-phase thermochemical composition vector need to be used.

In this work, the radiation flamelet/progress variable (RFPV) model for sooting flames developed by Mueller and Pitsch [97] is used. This model accounts for gas-phase radiation using an optically thin assumption. The gas-phase thermochemical composition vector $\boldsymbol{\phi}$ is parameterized using three variables, namely, mixture fraction (Z), a reaction progress variable (C) and a radiation heat loss parameter (H). Z is defined based on element mass fraction [98] while C is defined as a normalized sum of mass fractions of major product species. H is defined as the enthalpy deficit such that it describes the effect of heat loss on total enthalpy.

PAH formation is characterized by slow chemistry, and as discussed in Sec. 1.3, requires further consideration when a flamelet-based approach is used. In this work, a transport equation model is used for tracking unsteady PAH evolution [97, 99]. Transport equations for the variables representing the thermochemical composition vector in this approach are written as follows:

$$\frac{\partial \rho \boldsymbol{\kappa}}{\partial t} + \nabla \cdot \rho \mathbf{u} \boldsymbol{\kappa} = \nabla \rho D \cdot \nabla \boldsymbol{\kappa} + \rho \mathbf{S}(\boldsymbol{\kappa}), \tag{5.1}$$

where $\boldsymbol{\kappa} = [Z, C, H, \phi_{PAH}]$, and $\mathbf{S}(\boldsymbol{\kappa}) = [S_Z, S_C, S_H, S_{PAH}]$ represents appropriate source terms. ϕ_{PAH} is the total mass fraction of PAH compounds. Note that soot formation results in PAH removal from gas-phase leading to a source term in the continuity equation. As a result of this, a conserved scalar formulation cannot be used for mixture fraction, leading to the source term S_Z. In Eq. (5.1), $\rho S_H = \dot{\rho} H + \dot{q}_{RAD}$, where $\dot{q}_{RAD}$ is the radiation source term, while S_C and S_{PAH} are obtained directly from the flamelet library.

For constructing the flamelet library, flamelet equations [25] are solved and the solutions are stored in a table. In addition to the steady flamelet solutions, the RFPV approach includes unsteady flamelet solutions for parameterizing with respect to H. Further details of the RFPV approach can obtained from Mueller and Pitsch [97].

5.2 Volume/surface area based soot model

Evolution of soot is described using a population balance equation (PBE) for the soot number density function (NDF) $N(\boldsymbol{\zeta}; \mathbf{x}, t)$, where $\boldsymbol{\zeta}$ is a vector of internal coordinates. In order to account for fractal aggregates, two internal coordinates are used to describe the NDF: volume V and surface area S [38]. Since a direct solution to the PBE is computationally intractable, the soot population is represented by moments of the NDF:

$$M_{x,y} = \int V^x S^y N d\boldsymbol{\zeta}, \tag{5.2}$$

where x, y are the orders of the moment in volume and surface area, respectively. The transport equation for the moments obtained from the PBE using the above definition of moments (Eq. (5.2)) can be written as:

$$\frac{\partial M_{x,y}}{\partial t} + \nabla \cdot \mathbf{u} M_{x,y} = S^M_{x,y}(\boldsymbol{\zeta}, \boldsymbol{\phi}), \tag{5.3}$$

where $S^M_{x,y}$ represents the moment source terms accounting for nucleation, growth, and oxidation of soot particles, and $\boldsymbol{\phi}$ is a vector of thermochemical composition variables. A nucleation model based on dimerization of PAH [37, 100] is used in this study, and growth is modeled using the H-abstraction-C_2H_2-addition (HACA) mechanism [93]. Reaction rates proposed by Mueller *et al.* [101] are used for oxidation. Since only a finite number of moments are solved for, the moment source terms are unclosed. Closure is obtained with the hybrid method of moments (HMOM) [102]. The model is designed to capture the bimodality of the NDF while retaining numerical efficiency and robustness.

In HMOM, the contribution of the smaller particles to the moments is represented with a delta function, and the contribution of the large particles is represented with polynomial interpolation. Any moment of the soot NDF can then be written as

$$M_{x,y} = N_0 V_0^x S_0^y + M^R_{x,y} \ , \tag{5.4}$$

where, N_0, V_0 and S_0 are the weight and internal coordinates of the delta function. V_0 and S_0 are prescribed *a priori*, and a transport equation is solved

for N_0. $M_{x,y}^R$ is polynomial interpolation of order R [103]. In this work, a first-order interpolation is considered, and three moments, the soot number density $M_{0,0}$, volume $M_{1,0}$ and surface area $M_{0,1}$, are needed to determine the interpolation coefficients. The reader is referred to [102] for further details related to HMOM.

5.3 LES/PDF approach for soot modeling

In sooting flames, the state vector $\boldsymbol{\xi}$ that includes the gas-phase thermochemical composition vector $\boldsymbol{\kappa}$ and soot variables, needs to be tracked by solving transport equations. Specifically, $\boldsymbol{\xi} = [Z, C, H, \phi_{PAH}, M_{0,0}, M_{0,1}, M_{1,0}, N_0]$. In LES, a filtered form of these transport equations is written as follows:

$$\frac{\partial \overline{\rho}\widetilde{\boldsymbol{\xi}}}{\partial t} + \nabla \cdot \overline{\rho}\left(\widetilde{\mathbf{u}}\widetilde{\boldsymbol{\xi}} - (D + D_t)\nabla\widetilde{\boldsymbol{\xi}}\right) - \overline{\rho}\widetilde{\mathbf{S}}(\boldsymbol{\xi}) = 0, \tag{5.5}$$

where D_t is a turbulent diffusivity that is used to model the subfilter turbulent flux using the gradient diffusion hypothesis. Note that this equation is similar to the scalar transport equation (Eq. 2.9) discussed in Sec. 2.2, and the corresponding closure of the reaction source term $\widetilde{\mathbf{S}(\boldsymbol{\xi})}$ requires the joint-PDF of $\boldsymbol{\xi}$.

In the transported PDF approach, a partial differential equation describing the evolution of the joint-PDF in physical and compositional spaces is directly solved. The focus of this study is the simulation of a turbulent jet flame in cylindrical coordinates. For this purpose, the transport equation is

written in cylindrical coordinates as follows [104]:

$$\frac{\partial G_L}{\partial t} + \frac{\partial}{\partial r}\left[\left(A_r + \frac{B}{r}\right) G_L\right] + \frac{\partial}{\partial \theta}\left(\frac{A_\theta}{r} G_L\right) + \frac{\partial}{\partial z}\left(A_z G_L\right) + \frac{\partial^2}{\partial r^2}\left(B G_L\right) + \frac{\partial^2}{\partial \theta^2}\left(\frac{B}{r^2} G_L\right) + \frac{\partial^2}{\partial z^2}\left(B G_L\right) = -\frac{\partial}{\partial \vartheta_\alpha}\left[\left(\frac{1}{\overline{\rho}}\overline{\nabla \cdot \rho D \nabla \xi_\alpha | \boldsymbol{\vartheta}} + S_\alpha(\boldsymbol{\vartheta})\right)\frac{G_L}{r}\right] \tag{5.6}$$

where $F_L(\boldsymbol{\vartheta})$ is the joint-PDF of $\boldsymbol{\xi}$, $\boldsymbol{\vartheta}$ represents $\boldsymbol{\xi}$ in sample space, $G_L = rF_L$, and $B = D_t$. A_r, A_θ, and A_z are given by

$$A_r = \widetilde{u}_r + \frac{1}{\overline{\rho}}\frac{\partial}{\partial r}\left(\overline{\rho} B\right) \tag{5.7}$$

$$A_\theta = \widetilde{u}_\theta + \frac{1}{r\overline{\rho}}\frac{\partial}{\partial \theta}\left(\overline{\rho} B\right) \tag{5.8}$$

$$A_z = \widetilde{u}_z + \frac{1}{\overline{\rho}}\frac{\partial}{\partial z}\left(\overline{\rho} B\right). \tag{5.9}$$

Equation (5.6) can be obtained from Eq. (2.12) using coordinate transformation and a low Mach number assumption. As discussed in Sec. 2.3.1, the first term on the right-hand side represents conditional diffusion, and is modeled using the IEM model described in Eq. (2.14) and (2.15). Note that the differential diffusion between soot moments and the gas-phase scalars could be important [105]. As a first step, this is neglected here, but the differential diffusion of high-Schmidt number scalars could be considered by modifying the dissipation time scale [22, 106].

5.4 Numerical implementation in LES

The PDF approach is integrated with a low Mach number LES solver. The LES governing equations are solved in cylindrical coordinates using a

fractional time stepping procedure [107, 108]. A conservative finite difference approach is used for discretizing the nonlinear and viscous terms [109]. A Poisson equation system is used to enforce the continuity equation. Further details of the LES solver can be found in [109].

The transported PDF approach requires solution of the high-dimensional PDF transport equation (Eq. 5.6), which spans eleven dimensions for the state vector used in this work. As discussed in Sec. 2.3.2, conventional finite difference or finite volume methods are not tractable, and a Lagrangian Monte-Carlo method is used here [41–44, 50]. In the Lagrangian approach, the computational domain is seeded with a large number of notional particles that evolve in physical and compositional spaces using a set of stochastic differential equations. Each of these particles carries a property vector that consists of the particle location vector, a characteristic weight, and the $\boldsymbol{\xi}$ vector.

The evolution of the particles in physical space is governed by the following equations:

$$dr^n = \left(A_r^n + \frac{B_1^n}{r^n} \right) dt + \sqrt{2dtB_1^n} dW_r, \tag{5.10}$$

$$d\theta^n = \frac{A_\theta^n}{r^n} dt + \sqrt{2dt \frac{B_1^n}{\left(r^n\right)^2}} dW_\theta, \tag{5.11}$$

$$dz^n = A_z^n dt + \sqrt{2dtB_1^n} dW_z, \tag{5.12}$$

where the superscript n denotes the particle index, and $d\mathbf{W}$ is a Weiner diffusion process with zero mean and variance of 1, and $B_1 = D + D_t$. The velocity and diffusivity fields used in this equation are interpolated onto the

particle locations using trilinear interpolation. The transport in composition space consists of mixing and chemical reactions. The particle equation corresponding to the IEM mixing model is given by

$$d\boldsymbol{\vartheta}^n = \frac{1}{\tau}\left(\widetilde{\boldsymbol{\xi}} - \boldsymbol{\vartheta}^n\right), \tag{5.13}$$

where $\widetilde{\boldsymbol{\xi}}$ is the filtered composition vector in a given filter volume, $\boldsymbol{\vartheta}^n$ is the particle composition vector, and τ is a mixing time scale. In this work, the mixing time scale is determined using the local effective diffusivity and the filter scale (see Eq. 2.16), such that a model coefficient C_{mix} needs to be specified. The dynamic procedure proposed by Raman and Pitsch [44] is used for evaluating C_{mix}.

The particle equations thus reduce to solving a vector of ordinary differential equations.

$$d\boldsymbol{\vartheta}^n = \mathbf{S}(\boldsymbol{\vartheta}^n)dt, \tag{5.14}$$

where $\mathbf{S}(\boldsymbol{\vartheta})$ is the vector of source terms defined in Eq. (5.5), and is obtained from precomputed flamelet libraries and local values of ϕ_{PAH}, $M_{x,y}$ and N_0.

The particle weights are proportional to the mass of the fluid they represent. It should be noted that the PDF transport equation is formulated for rF_L instead of F_L. This modified formulation ensures that the weights have no evolution equation. In other words, the particle weights are initialized at the inlet but do not change with time. To ensure consistency, the particle weights are set proportional to $\overline{\rho}^n r_0^n$ at the inlet, where $\overline{\rho}^n$ is the Eulerian

density interpolated to the particle location, and r_0^n is the radial location of the particle.

5.5 Summary

The modeling framework necessary for simulating sooting turbulent flames was presented in this chapter. The three primary components of this framework include the RFPV approach for chemistry modeling, bivariate soot NDF for soot particle dynamics, and LES/PDF approach for turbulence. In the next chapter, these are used for predicting soot formation in an experimental flame.

Chapter 6

LES/PDF studies of turbulent sooting flame

In this chapter, the PDF approach discussed in Chapter 5 is validated using an experimental piloted flame. The experimental flame configuration is first described. This is followed by results from the computational study, with emphasis on subfilter gas phase-soot correlations.

6.1 Delft flame: Simulation details

Delft Flame III [110] is a piloted turbulent jet diffusion flame fueled by commercial natural gas. The use of natural gas results in a non-sooting region near the burner and a downstream moderately sooting region. The burner consists of a central fuel jet with a diameter of 6 mm surrounded by an annulus of air with an inner diameter of 15 mm and an outer diameter of 45 mm [111]. The fuel velocity is 21.9 m/s, and the air velocity is 4.4 m/s. Twelve circular pilot flames with diameters of 0.5 mm are situated on a ring between the fuel jet and the air annulus with a diameter of 7 mm. In the simulation, the pilot is modeled as an annulus with a width equal to the diameter of the individual pilots in the actual burner. The burner assembly is surrounded by a slow co-flow of air with a velocity of 0.3 m/s.

Three sets of experimental measurements have been made with the burner. In the near-burner region where soot is not present, velocity measurements were made by Stroomer [112], and temperature and species mass fractions were measured by Nooren *et al.* [111]. More recently, soot volume fraction was measured in the downstream region by Qamar *et al.* [13].

A $384 \times 192 \times 64$ grid clustered near the jet shear layers, and spanning $150d \times 43d$ in the axial and radial directions is used, where d is the jet diameter. Transient inflow velocity profiles for the central jets (fuel and air) are obtained from separate simulations of the burner geometry. The co-flow is prescribed as a bulk flow. For chemical kinetics, a detailed 158 species mechanism developed by Narayanaswamy *et. al.* [96] has been used with modifications from Mueller and Pitsch [97]. The flamelet lookup library is constructed using Flamemaster [113], and is stored in a lookup table spanning $100 \times 50 \times 35$ points in Z, C, and H directions, respectively. This study was conducted using 256 CPU cores for roughly 400 hours, during which statistics were collected over approximately 100 ms.

6.2 Results and Discussion

6.2.1 Instantaneous fields

Figure 6.1 shows the instantaneous fields of temperature, PAH mass fraction, soot volume fraction, and soot number density. As expected, soot formation is predominant in the fuel-rich region inside the stoichimetric surface where moderately high temperatures aid the formation of PAH molecules.

While PAH formation is initiated far upstream ($x/d > 20$), significant soot volume fraction is observed only after $x/d = 60$. The lag between PAH growth and soot formation shows the time scale differences between the two processes. Similar to the experiment, soot formation is found to be highly intermittent with sporadic bursts of high soot volume fraction regions followed by extended periods of low soot volume fraction. Prior studies have demonstrated that soot precursor growth, especially the evolution of naphthalene, is highly sensitive to the strain rates in the flow. Consequently, the turbulent features that a fluid packet experiences strongly dictates soot nucleation [114]. Figure 6.1 also shows that the soot number density starts to increase far upstream due to nucleations up to $x/d = 20$. Further downstream, the number density remains remains essentially constant, while soot volume fraction increases drastically, indicating significant particle growth assisted primarily by coagulation and PAH condensation. Finally, at $x/d > 80$, oxidation dominates and quickly eliminates soot

6.2.2 Soot and gas-phase statistics

Figure 6.2 shows the time-averaged mixture fraction and temperature statistics for the flame, measured far upstream of the region of high soot volume fraction. Results indicate that the LES/PDF predicts the flame statistics reasonably accurately, including the RMS statistics of the flow. In the transported PDF approach, the subfilter mixing model (Eq. 5.13) is a source of spatial numerical diffusion since it mixes particles that are spatially distributed

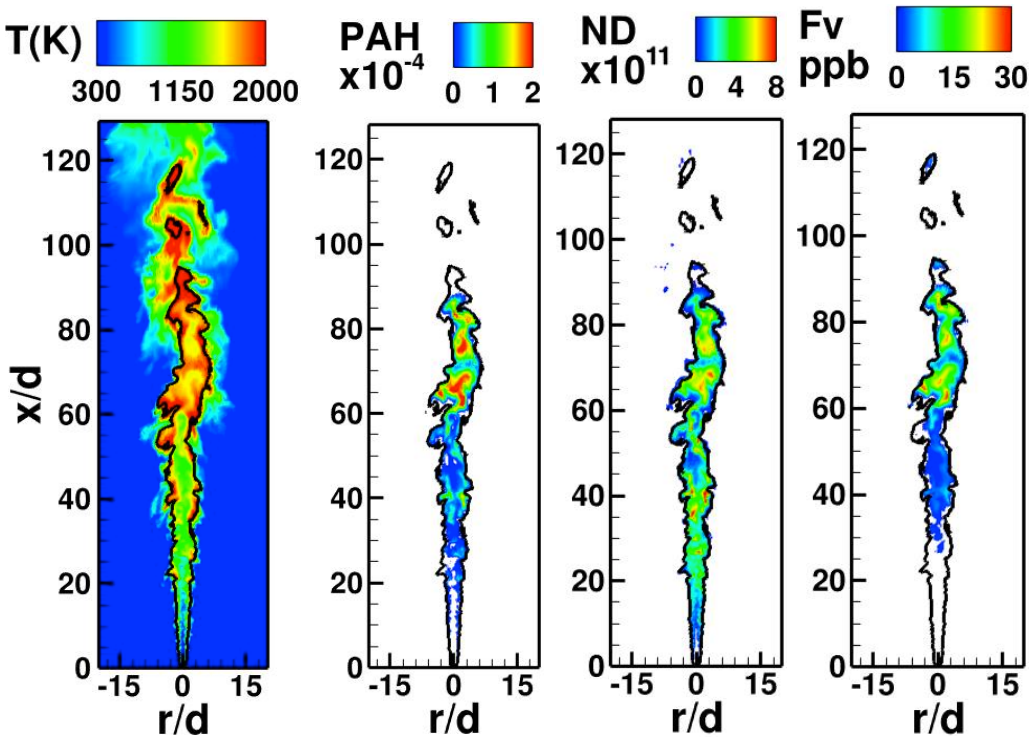

Figure 6.1: Instantaneous contours of temperature, PAH mass fraction, soot volume fraction, and soot number density. Iso-value of stoichiometric mixture fraction is indicated by a solid black line.

within a single control volume. As the dissipation rate increases, the higher mixing rates lead to increased numerical diffusion that will manifest as reduced temporal fluctuations. The accuracy of the RMS statistics provides confidence that the PDF numerics have not unduly affected the flame computation.

Figure 6.3 shows the mixture fraction and soot volume fraction obtained from the LES/PDF approach and the experiments. The simulation results overpredict the soot volume fraction substantially, and also show an earlier inception and growth compared to the experiments. Mueller and Pitsch [97] reported that the magnitude of soot profiles displayed large sensitivity to the dissipation rate models used. Here, a dynamic procedure is used to evaluate the dissipation rate [44]. While this approach was shown to correctly predict extinction levels in partially-premixed flames, LES models that depend on scalar gradients are susceptible to high numerical errors [72, 73], which would partially explain the over prediction here. The location of inception, however, is not affected by dissipation rate but is more sensitive to the chemistry model [97].

Although the scalar comparisons upstream (Fig. 6.2) are reasonably good, it is not known if the minor errors seen upstream will propagate and amplify further downstream. For instance, the mixture fraction plots show an over-prediction of roughly 15% near the centerline, while the temperature itself is nearly the same as experiments. This mismatch could lead to fuel-rich high temperature regions downstream that will promote the formation of soot particles. Without further information on the scalar profiles downstream, it is

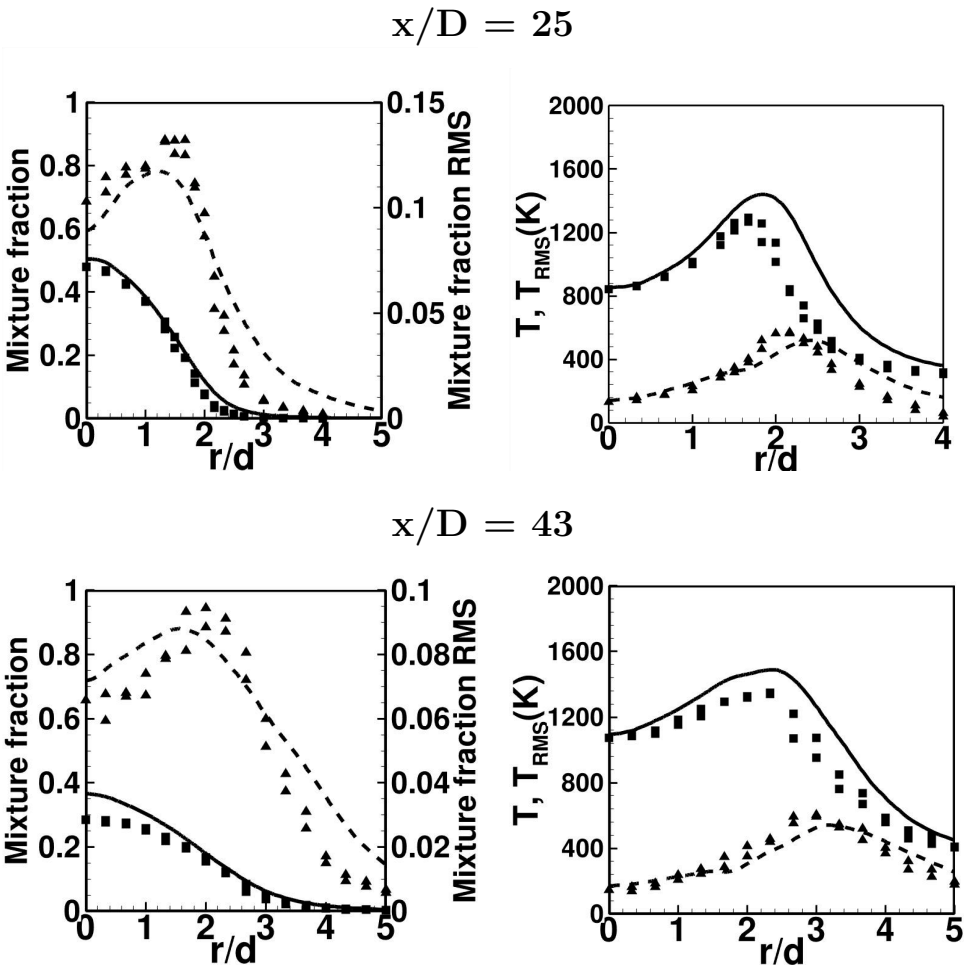

Figure 6.2: Comparison of time averaged mean and RMS of mixture fraction and temperature with the experiment of Nooren, *et. al.* [111]. Simulation: mean (—), RMS (- - - -); Experiment: mean (■), RMS (▲).

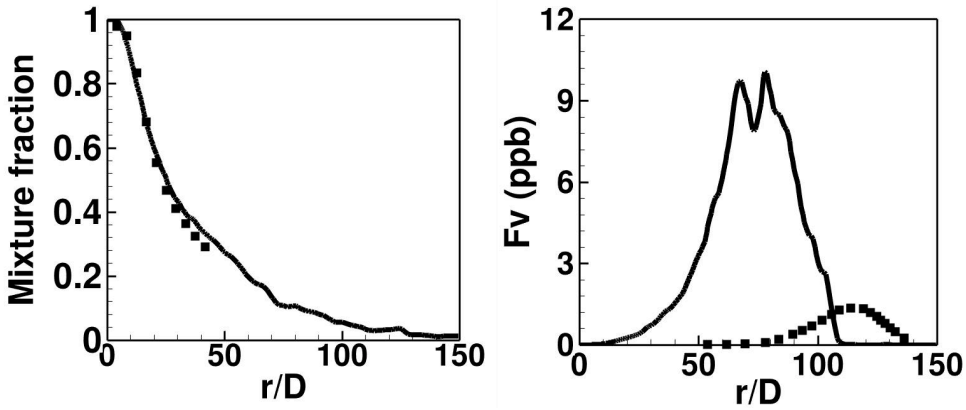

Figure 6.3: Comparison of mixture fraction and soot volume fraction from the simulation with the experiments of Nooren, *et al.* [111] and Qamar, *et al.* [13] respectively. The data is plotted along the centerline.

not possible to deduce the role of these errors in prediction errors.

6.2.3 Subfilter soot and scalar statistics

From the particle information, subfilter statistics and PDFs can be computed to better understand soot evolution. Figure 6.4 shows the instantaneous contours of subfilter standard deviation of mixture fraction, temperature, soot volume fraction, and number density. It is seen that the subfilter fluctuations of mixture fraction are confined to the near-stoichiometric region, with the variations essentially reduced to zero outside of this region. While temperature fluctuations follow a similar pattern, the high standard deviation regions are seen on the lean-side of the flame, outside the closed surface formed by the stoichiometric contour. Due to the large gradient of temperature in mixture fraction space, small fluctuations in mixture fraction lead to large changes

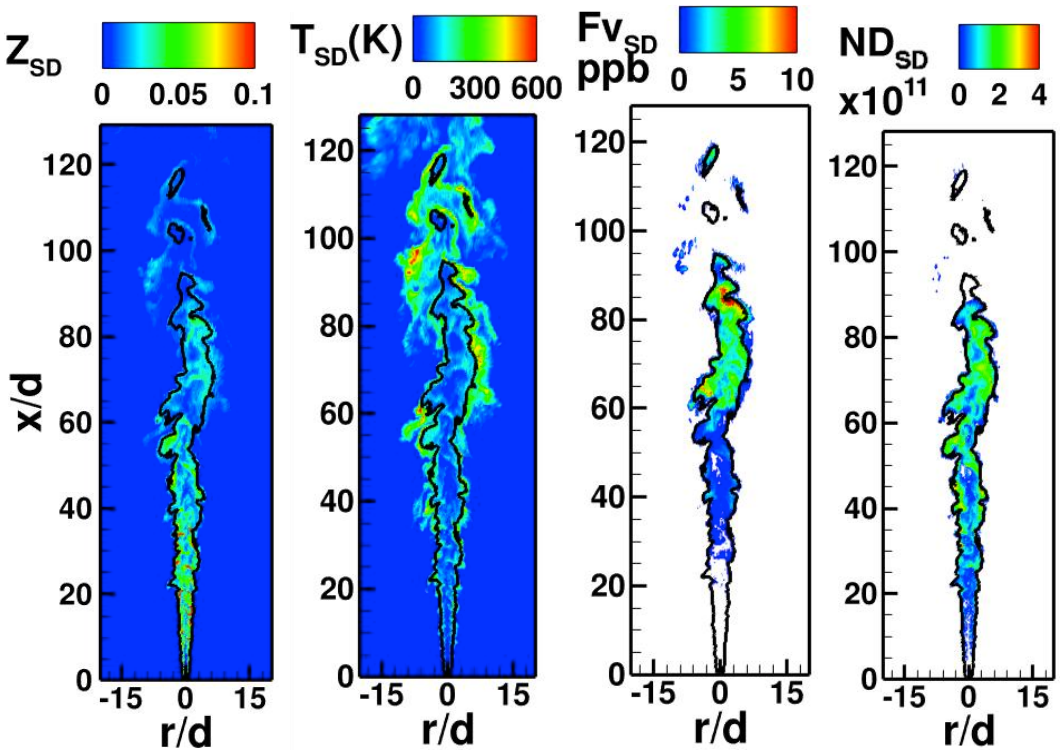

Figure 6.4: Instantaneous contours of subfilter standard deviation of mixture fraction, temperature, soot number density and soot volume fraction. Iso-value of stoichiometric mixture fraction is indicated by a solid black line.

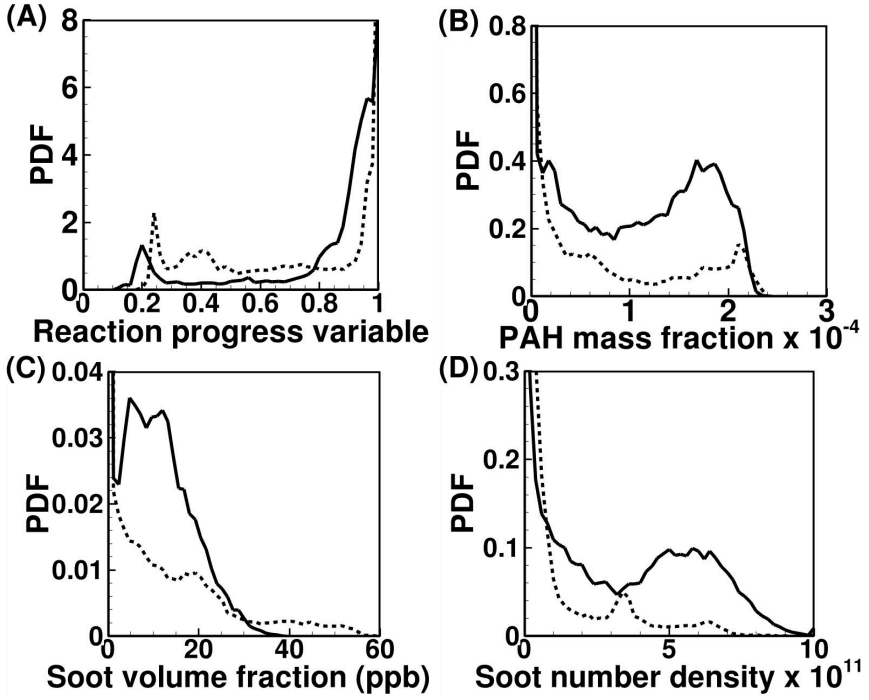

Figure 6.5: Time averaged marginal PDFs of **(a)** reaction progress variable, **(b)** PAH mass fraction, **(c)** soot mass fraction, and **(d)** soot number density plotted at $r/d = 1.5$. $x/d = 70$: (—), $x/d = 90$: (- - - -). For averaging, data from multiple instantaneous fields was used.

in temperature in lean mixtures. The subfilter fluctuations of soot moments are also large, reaching as high as 40% of the mean values. Similar to the filtered moments, the peaks in these quantities are located in the relatively high-temperature fuel-rich regions inside the stoichiometric surface.

Figure 6.5 shows the time-averaged PDF of scalars computed at different axial locations, slightly off the centerline. Here, data sets at several instances, spanning more than 70 ms, have been used to obtain time-averaged

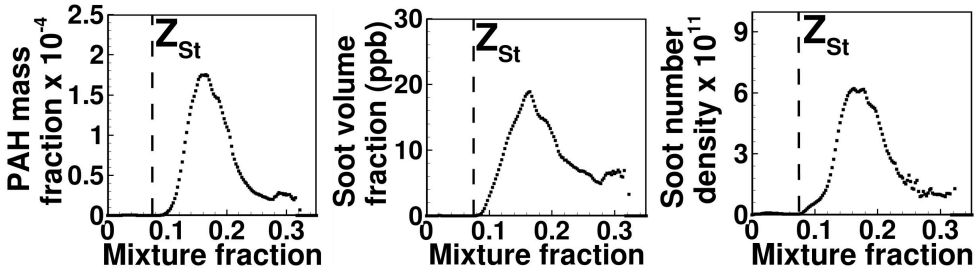

Figure 6.6: Time averaged conditional plots of PAH mass fraction, soot volume fraction and soot number density plotted at $x/d = 70$. For averaging, data from multiple instantaneous fields was used.

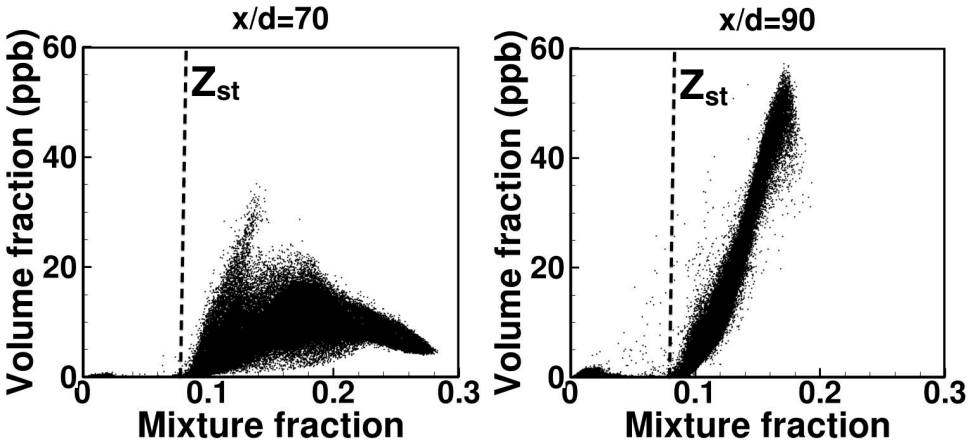

Figure 6.7: Instantaneous scatter plot of soot volume fraction versus mixture fraction plotted at $x/d = 70$ (left) and $x/d = 90$ (right).

distribution functions. In this sense, the PDF is not a true sub-filter quantity, which would require conditioning on the filtered field [23, 115]. Note that $x/d = 70$ represents the axial plane with highest soot volume fraction in the simulation (see Fig. 6.3). The progress variable is skewed towards the values greater than 0.8, indicating a fully burning mixture. The mixture fraction PDF (not shown here) shows a broader spread, with significant probability of having fuel-rich pockets. The PAH PDF shows a bi-modal behavior with a large fraction of the particles having near-zero PAH concentrations and another group of particles with higher PAH values. These two groups of particles come from the fuel-lean and fuel-rich sides, respectively, corresponding to the broad mixture fraction PDF observed. The PDF of soot moments exhibits a broad and nearly uniform PDF, with a bias towards zero moment corresponding to the fuel-lean mixture fraction values.

6.2.4 Conditional statistics

The evolution of the soot particles in mixture fraction and reaction progress variable coordinates is illustrative of the evolution process. Figure 6.6 shows time averaged plots of PAH mass fraction, soot volume fraction and soot number density, conditioned on mixture fraction, at $x/d = 70$. All three quantities show a peak in values near a mixture fraction of 0.165, which seems to be the most likely fuel composition to contain soot. It is also seen that there is a near linear increase in the quantities in the region of $0.075 < Z < 0.16$, but the profiles have a non-linear shape in richer mixtures. To further under-

stand these conditional statistics, Fig. 6.7 shows the instantaneous conditional scatter plot at two different locations (at the same instance as that in Figs. 6.1 and 6.4). It is seen that when the filtered soot volume fraction is lower (< 20 ppb), the conditional plots show a wider spread with richer regions containing significant soot volume fractions. Here, the mixture fraction PDF itself is broader, with a wider range of values present. However, when the filtered soot volume fraction is higher ($x/d = 90$), the mixture fraction distribution appears narrower, and the conditional scatter plot exhibits a linear profile. These two modes result in the behavior seen in Fig. 6.6.

Figure 6.8 shows the two-dimensional scatter plots of PAH mass fraction and soot volume fraction in $\{Z, C\}$ space. The plots show that PAH is significantly higher in a small region with very high progress variable in the fuel-rich region. Soot volume fraction, on the other hand, has a wider spread with large soot volume fractions seen in regions of lower progress variable (and lower temperature) inside the fuel-rich region. This indicates that the soot particles travel away from the region of high PAH concentration. Some of this soot formation could be due to surface growth, which is independent of PAH concentration. It is also important to note that these conditional statistics are sensitive to the subfilter mixing model used. Since soot particles do not diffuse, the assumption of equal diffusivities will have some impact on the results obtained here. In particular, soot oxidation in the near-stoichiometric region should be higher than that seen in this simulation. Since the IEM model allows the notional particles to mix without reacting thereby allowing

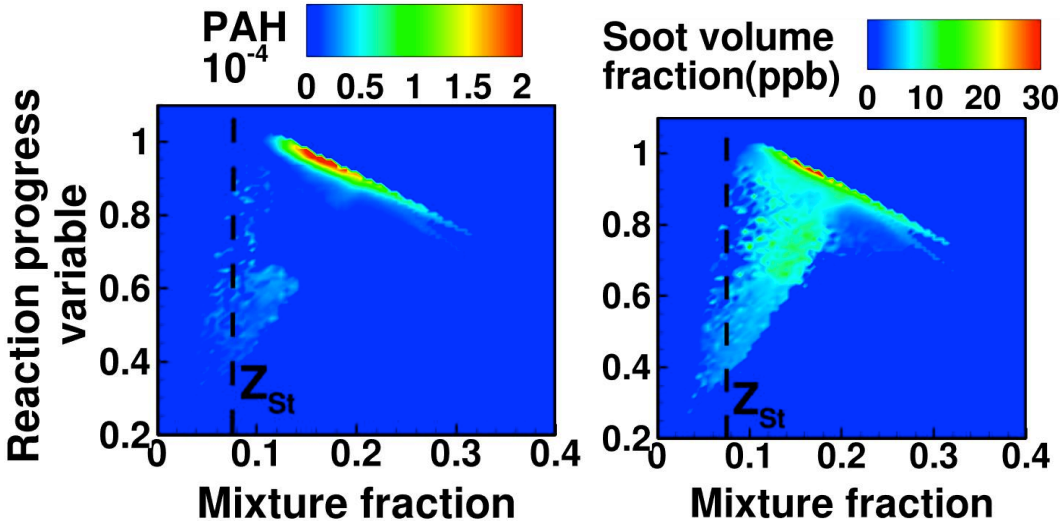

Figure 6.8: Time averaged contours of PAH mass fraction and soot volume fraction conditioned on mixture fraction and reaction progress variable plotted at $x/d = 70$. For averaging, data from multiple instantaneous fields was used.

traversal in composition space across flame fronts, the effect of oxidation is under-predicted. The influence of differential diffusion on soot evolution needs further consideration.

6.3 Conclusions

The LES/PDF approach was used to simulate turbulent sooting flames. Detailed gas-phase precursor kinetics were included using an extended flamelet/ progress variable approach that accounts for radiation effects as well as unsteady PAH formation. While the LES computations over-predicted soot volume fraction compared to experiments, it qualitatively reproduced the soot profiles by recreating the gradual increase in soot volume fraction through

inception and growth, followed by a quick decrease due to oxidation. The quantitative error in predictions can be attributed to errors in modeling subfilter dissipation in the PDF approach, the flamelet-based gas-phase chemistry approximation, and uncertainties in reaction rates for dimer and PAH formation. The subfilter standard deviation of soot moments is comparable to the filtered values. The subfilter PDF of soot moments shows a broad spread with a bias towards zero soot content, consistent with the highly intermittent soot formation observed in these flames. Further, conditional statistics show significant scatter of soot moments with respect to mixture fraction. In general, the peak in soot volume fraction occurs close to a mixture fraction value of 0.165, whereas the stoichiometric mixture fraction is only 0.075. In the flow configuration considered, modeled soot is formed far downstream where turbulent fluctuations are weaker compared to the near-nozzle locations. The conditional statistics from the model show that PAH is confined to a narrow region in mixture fraction/ progress variable space, while the soot moments show broader spread.

Chapter 7

Conclusion and future direction

The LES/PDF approach offers a comprehensive methodology for simulating turbulent reacting flows. In the past, this approach had been demonstrated in low Mach number flows involving purely gas-phase combustion. The primary contribution of this dissertation is to extend the applicability of LES/PDF methods towards studying supersonic shock-containing flows inside scramjet combustors, and sooting turbulent flows involving reactions with particulate matter. In this chapter, conclusion from the supersonic combustion work are presented, followed by deductions from the soot modeling research. Finally, possible directions for future extension of this work have been discussed.

7.1 Supersonic combustion modeling studies

Quadrature based methods like DQMOM provide a computationally feasible means for solving the PDF transport equation. Deterministic and Eulerian nature of these methods permits easy implementation in to standard CFD solvers, and enable the application of PDF methods in complex geometries and realistic flow configurations. The effect of discretization errors on

the evolution of the PDF however needs to be considered when these methods are implemented in LES. Specifically, transport equations in DQMOM are obtained under the assumption of smooth scalar fields. These assumption expectedly break down in the presence of steep gradients. As a result, the evolution of the PDF is prone to errors in flows with non-premixed or partially premixed combustion.

In this work, an alternative SeQMOM approach was developed. This new method is based on a conservative moment-based formulation, and is therefore not prone to discretization based errors observed in DQMOM. For robustness, SeQMOM equations are solved simultaneously with DQMOM such that the DQMOM solution is used in regions of low variance. Nonetheless, even this hybrid approach was shown to be significantly more accurate in comparison with DQMOM. Also, the computational cost of using the new approach is significantly lower than the conventional Monte Carlo methods, making complex combustor studies computationally tractable. Further, the SeQMOM technique can be easily integrated into existing flow solvers. Since the SeQMOM equations are identical to scalar transport equations, the methodology is highly scalable on parallel computers.

7.2 Soot modeling studies

For soot modeling, the LES/PDF approach was coupled with detailed models for soot formation and growth. A Lagrangian Monte Carlo approach was used for solving the PDF transport equation, leading to detailed informa-

tion about subfilter correlations between soot and the gas phase composition. Statistics of soot volume fraction and PAH mass fraction were highly correlated, conveying that PAH played a significant role in soot particle growth. Also, subfilter soot statistics showed a wide spread, implying simplifying assumptions about these quantities in LES will lead to significant errors. Finally, marginal PDFs of soot and PAH highlighted the intermitted behavior that characterizes soot evolution.

7.3 Future directions

7.3.1 SeQMOM using partial Beta and Gaussian PDF

Quadrature based methods use weighted delta peaks for representing the true PDF. While these methods have been shown to represent PDFs having low variance with a reasonable amount of accuracy, for representing PDFs with high variance, a large number of quadrature point could be required. Numerical implementation of higher order quadrature leads to problems with ill-conditioned moments. A promising alternative is provided by using partial Beta or Gaussian PDFs. Preliminary studies have indicated that such an approach could potentially lead to a significant gain in accuracy without any increase in computational cost. A future study should therefore include development of SeQMOM based on partial Beta and Gaussian PDFs.

7.3.2 LES/PDF modeling of soot with differential diffusion

In the soot modeling studies, a unity Lewis number approximation has been used. However, differential diffusion between soot moments and the gas-phase scalars could be important [105], potentially influencing transport of soot in mixture fraction space [116]. A future study could therefore investigate the effect of differential diffusion by using formulations proposed by McDermott and Pope [117], and Richardson and Chen [118].

Appendix

Appendix A

PDF transport equation

A transport equation for the joint-PDF of the thermochemical composition vector is a central component in PDF methods. In this appendix, the composition-sensible enthalpy joint-PDF transport equation is derived from first principles.

Based on the definition of the PDF in Eq. (2.10), filtered value of any random field $B(\boldsymbol{\phi})$ can be written as

$$\widetilde{B(\boldsymbol{\phi})} = \frac{1}{\overline{\rho}} \int B(\boldsymbol{\psi}) F d\boldsymbol{\psi}, \tag{A.1}$$

where $\boldsymbol{\psi}$ represents the random thermochemical composition vector $\boldsymbol{\phi}$ in sample space, and $\overline{\rho}$ is the filtered value of density. Similarly,

$$\begin{aligned} \widetilde{\mathbf{u}B(\boldsymbol{\phi})} &= \frac{1}{\overline{\rho}} \int B(\boldsymbol{\psi}) \mathbf{v} f_{\mathbf{v},\boldsymbol{\psi}} d\mathbf{v} d\boldsymbol{\psi} \\ &= \frac{1}{\overline{\rho}} \int B(\boldsymbol{\psi}) \widetilde{\mathbf{u}|\boldsymbol{\psi}} F d\boldsymbol{\psi}, \end{aligned} \tag{A.2}$$

where $\mathbf{v}$ is the sample space variable representing the velocity field $\mathbf{u}$, and $f_{\mathbf{v},\boldsymbol{\psi}}$ is the joint-PDF of velocity, composition and sensible enthalpy. Further, $\overline{\rho}\widetilde{\mathbf{u}|\boldsymbol{\psi}} = \int \mathbf{v} f_{\mathbf{v}|\boldsymbol{\psi}} d\mathbf{v} d\boldsymbol{\psi}$, and using the Bayes' theorem [119], $\overline{\rho} f_{\mathbf{v},\boldsymbol{\psi}} = F f_{\mathbf{v}|\boldsymbol{\psi}}$.

Using this, a filtered transport equation for $B(\boldsymbol{\psi})$ can be written as

$$\frac{\partial \overline{\rho}\widetilde{B(\boldsymbol{\phi})}}{\partial t} + \nabla \cdot \overline{\rho}\widetilde{\mathbf{u}B(\boldsymbol{\phi})} = \int B(\boldsymbol{\psi}) \left(\frac{\partial F}{\partial t} + \nabla \cdot \widetilde{\mathbf{u}|\boldsymbol{\psi}} F \right). \tag{A.3}$$

Next, using the continuity equation (Eq. 2.5) and a chain rule,

$$\begin{aligned} \frac{D\widetilde{B(\boldsymbol{\phi})}}{Dt} &= \frac{\partial \widetilde{B(\boldsymbol{\phi})}}{\partial \boldsymbol{\phi}} \frac{D\boldsymbol{\phi}}{Dt} \\ &= \frac{\partial \widetilde{B(\boldsymbol{\phi})}}{\partial \boldsymbol{\phi}} \widetilde{E(\boldsymbol{\phi}, \mathbf{x})}, \end{aligned} \tag{A.4}$$

where $E(\boldsymbol{\phi}, \mathbf{x})$ represents the entire right hand side of Eq. (2.1) and (2.2), and $\mathbf{x}$ is the spatial coordinate. Further simplifying Eq. (A.4), we get

$$\begin{aligned} \frac{D\widetilde{B(\boldsymbol{\phi})}}{Dt} &= \frac{1}{\overline{\rho}} \int \frac{\partial B(\boldsymbol{\phi})}{\partial \boldsymbol{\phi}} E(\boldsymbol{\phi}, \mathbf{x}) f_{\boldsymbol{\psi},\mathbf{y}} d\boldsymbol{\psi} d\mathbf{y} \\ &= \frac{1}{\overline{\rho}} \int Q(\boldsymbol{\psi}) \frac{\partial}{\partial \boldsymbol{\psi}} \widetilde{E|\boldsymbol{\psi}} F d\boldsymbol{\psi}. \end{aligned} \tag{A.5}$$

Here, $\mathbf{y}$ is a sample space variable representing $\mathbf{x}$, and $f_{\boldsymbol{\psi},\mathbf{y}}$ is the multipoint joint-PDF of $\boldsymbol{\psi}$. Finally, using Eq. (2.1), (2.2), (A.3) and (A.5), we get

$$\begin{aligned} \frac{\partial F}{\partial t} + \nabla \cdot \widetilde{\mathbf{u}|\boldsymbol{\psi}} F = &- \frac{\partial}{\partial \psi_\alpha} \left(\left[\frac{1}{\overline{\rho}} \overline{\nabla \cdot \rho D \nabla \phi_\alpha | \boldsymbol{\psi}} + S_\alpha(\boldsymbol{\psi}) \right] F \right) \\ &- \frac{\partial}{\partial \psi_h} \left(\frac{1}{\overline{\rho}} \overline{\left[\frac{Dp}{Dt} + \boldsymbol{\tau} : \mathbf{S} \right] | \boldsymbol{\psi}} \; F \right) \end{aligned} \tag{A.6}$$

Note that in the above equation, while the reaction source term $\mathbf{S}(\boldsymbol{\phi})$ is in closed form, all conditionally averaged terms need to be modeled. This has been further discussed in Sec. 2.3.1.

Bibliography

[1] NASA. *How scramjets work. http : //www.nasa.gov/centers/langley /news/factsheets/X43A_2006_5.html*, February 2006.

[2] MR Gruber, AS Nejad, TH Chen, and JC Dutton. Mixing and penetration studies of sonic jets in a Mach-2 freestream. *Journal of propulsion and power*, 11(2):315–323, Mar-Apr 1995.

[3] WM VanLerberghe, JG Santiago, JC Dutton, and RP Lucht. Mixing of a sonic transverse jet injected into a supersonic flow. *AIAA Journal*, 38(3):470–479, Mar 2000.

[4] A. Ben-Yakar and R.K. Hanson. Experimental investigation of flame-holding capability of hydrogen transverse jet in supersonic cross-flow. *Symposium (International) on Combustion*, 27(2):2173 – 2180, 1998.

[5] A. Ben-Yakar, M. G. Mungal, and R. K. Hanson. Time evolution and mixing characteristics of hydrogen and ethylene transverse jets in supersonic crossflows. *Physics of Fluids*, 18(2):026101, 2006.

[6] JM Seiner, SM Dash, and DC Kenzakowski. Historical survey on enhanced mixing in scramjet engines. *Journal of Propulsion and Power*, 17(6):1273–1286, Nov-Dec 2001.

[7] DW Bogadnoff. Adavnces injection and mixing techniques for Scramjet combustors. *Journal of Propulsion and Power*, 10(2):183–190, MAR-APR 1994.

[8] Valerio Viti, Reece Neel, and Joseph A. Schetz. Detailed flow physics of the supersonic jet interaction flow field. *Physics of Fluids*, 21(4), APR 2009.

[9] A Ben-Yakar and RK Hanson. Cavity flame-holders for ignition and flame stabilization in scramjets: An overview. *Journal of Propulsion and Power*, 17(4):869–877, JUL-AUG 2001. AIAA/ASME/SAE/ASEE 34th Joint Propulsion Conference and Exhibit, Cleveland, Ohio, JUL 12-15, 1998.

[10] Wei Huang, Mohamed Pourkashanian, Lin Ma, Derek B. Ingham, Shi Bin Luo, and Zhen Guo Wang. Investigation on the flameholding mechanisms in supersonic flows: backward-facing step and cavity flameholder. *Journal of Visualization*, 14(1):63–74, FEB 2011.

[11] D. J. Micka and J. F. Driscoll. Combustion characteristics of a dual-mode scramjet combustor with cavity flameholder. *Proceedings of the combustion institute*, 32:2397–2404, 2009.

[12] Heeseok Koo, Pratik Donde, and Venkat Raman. LES-based Eulerian PDF approach for the simulation of scramjet combustors. *Proceedings of the Combustion Institute*, 2012.

[13] N. H. Qamar, Z. T. Alwahabi, Q. N. Chan, G. J. Nathan, D. Roekaerts, and K. D. King. Soot volume fraction in a piloted turbulent jet non-premixed flame of natural gas. *Combustion and Flame*, 156(7):1339–1347, JUL 2009.

[14] S. B. Pope. *Turbulent Flows*. Cambridge University Press, 2000.

[15] F. M. White. *Fluid Mechanics*. McGraw Hill, 2003.

[16] Parviz Moin and Krishnan Mahesh. Direct numerical simulation: A tool in turbulence research. *Annual Review of Fluid Mechanics*, 30(1):539–578, 1998.

[17] Takashi Ishihara, Toshiyuki Gotoh, and Yukio Kaneda. Study of high-reynolds number isotropic turbulence by direct numerical simulation. *Annual Review of Fluid Mechanics*, 41(1):165–180, 2009.

[18] R. D. Moser, J. Kim, and N. N. Mansour. Direct numerical simulation of turbulent channel flow up to Re=590. *Physics of Fluids*, 11:943–945, April 1999.

[19] Hung Le, Parviz Moin, and John Kim. Direct numerical simulation of turbulent flow over a backward-facing step. *Journal of Fluid Mechanics*, 330:349–374, 1997.

[20] Xiaohua Wu and Parviz Moin. A direct numerical simulation study on the mean velocity characteristics in turbulent pipe flow. *Journal of Fluid Mechanics*, 608:81–112, 2008.

[21] M. R. Overholt and S. B. Pope. Direct numerical simulation of a statistically stationary, turbulent reactive flow. *Combustion Theory and Modelling*, 3:371–408, 1999.

[22] R. O. Fox. *Computational Models for Turbulent Reacting Flows*. Cambridge University Press, Cambridge, 2003.

[23] H. Pitsch. Large-eddy simulation of turbulent combustion. *Annual Review of Fluid Mechanics*, 38:453–482, 2006.

[24] N. Peters. Laminar diffusion flamelet models in non-premixed turbulent combustion. *Progress in Energy and Combustion Science*, 10(3):319 – 339, 1984.

[25] Norbert Peters. *Turbulent Combustion*. Cambridge University Press, 2000.

[26] J. Jimenez, A. Linan, M. M. Rogers, and F. J. Higuera. *A Priori* testing of subgrid models for chemically reacting non-premixed turbulent flows. *Journal of Fluid Mechanics*, 349:149–171, 1997.

[27] A. W. Cook, J. J. Riley, and G. Kosály. A laminar flamelet approach to subgrid-scale chemistry in turbulent flows. *Combustion and Flame*, 109:332–341, 1997.

[28] A. Kempf, R.P. Lindstedt, and J. Janicka. Large-eddy simulation of a bluff-body stabilized nonpremixed flame. *Combustion and Flame*, 144(12):170 – 189, 2006.

[29] H. Pitsch and N. Peters. A consistent flamelet formulation for non-premixed combustion considering differential diffusion effects. *Combustion and Flame*, 114(12):26 – 40, 1998.

[30] H. Pitsch. Unsteady flamelet modeling of differential diffusion in turbulent jet diffusion flames. *Combustion and Flame*, 123:358–374, 2000.

[31] T. Poinsot and D. Veynante. *Theoretical and Numerical Combustion*. R. T. Edwards, Philadelphia, USA, 2001.

[32] F. M. White. *Viscous Fluid Flow*. McGraw Hill, 1991.

[33] M. Germano. Turbulence : The filtering approach. *Journal of Fluid Mechanics*, 286:229–255, 1991.

[34] A. T. Hsu, Y.-L. P. Tsai, and M. S. Raju. Probability density function approach for compressible turbulent reacting flows. *AIAA Journal*, 32:1407–1415, July 1994.

[35] Heeseok Koo, Pratik Donde, and Venkat Raman. A quadrature-based LES/transported probability density function approach for modeling supersonic combustion. *Proceedings of the Combustion Institute*, 33(2):2203 – 2210, 2011.

[36] Pratik Donde, Heeseok Koo, and Venkat Raman. A multivariate quadrature based moment method for LES based modeling of supersonic combustion. *Journal of Computational Physics*, 231(17):5805 – 5821, 2012.

[37] G. Blanquart and H. Pitsch. Analyzing the effects of temperature on soot formation with a joint volume-surface-hydrogen model. *Combustion and Flame*, 156(8):1614 – 1626, 2009.

[38] Michael Edward Mueller, Guillaume Blanquart, and Heinz Pitsch. A joint volume-surface model of soot aggregation with the method of moments. *Proceedings of the Combustion Institute*, 32(1):785 – 792, 2009.

[39] A. Schild, A. Gutsch, H. Mhlenweg, and S.E. Pratsinis. Simulation of nanoparticle production in premixed aerosol flow reactors by interfacing fluid mechanics and particle dynamics. *Journal of Nanoparticle Research*, 1:305–315, 1999.

[40] Janine Chungyin Cheng and Rodney O. Fox. Kinetic modeling of nanoprecipitation using CFD coupled with a population balance. *Industrial and Engineering Chemistry Research*, 49(21):10651–10662, 2010.

[41] F. A. Jaberi, P. J. Colucci, S. James, P. Givi, and S. B. Pope. Filtered mass density function for large-eddy simulation of turbulent reacting flows. *Journal of Fluid Mechanics*, 401:85–121, 1999.

[42] P. J. Colucci, F. A. Jaberi, and P. Givi. Filtered density function for large eddy simulation of turbulent reacting flows. *Physics of Fluids*, 10(2):499–515, 1998.

[43] V. Raman, H. Pitsch, and R. O. Fox. A consistent hybrid LES-FDF scheme for the simulation of turbulent reactive flows. *Combustion and*

Flame, 143(1-2):56–78, 2005.

[44] V. Raman and H. Pitsch. A consistent LES/filtered-density function formulation for the simulation of turbulent flames with detailed chemistry. *Proceedings Proceedings of the Combustion Institute*, 31:1711–1719, 2006.

[45] S. B. Pope. PDF methods for turbulent reactive flows. *Progress in Energy and Combustion Science*, 11:119, 1985.

[46] Pratik Donde, Venkat Raman, Michael E. Mueller, and Heinz Pitsch. LES/PDF based modeling of sootturbulence interactions in turbulent flames. *Proceedings of the Combustion Institute*, 2012.

[47] Daniel W. Meyer and Patrick Jenny. Micromixing models for turbulent flows. *Journal of Computational Physics*, 228(4):1275 – 1293, 2009.

[48] Kuochen Tsai and Rodney O. Fox. Modeling multiple reactive scalar mixing with the generalized IEM model. *Physics of Fluids*, 7(11):2820–2830, November 1995.

[49] Zhuyin Ren and Stephen B. Pope. An investigation of the performance of turbulent mixing models. *Combustion and Flame*, 136(12):208 – 216, 2004.

[50] S. B. Pope. A Monte Carlo method for the PDF equations of turbulent reactive flow. *Combustion Science and Technology*, 25:159–174, 1981.

[51] C. Dopazo. Relaxation of initial probability density function in the turbulent connection of scalar fields. *Physics of Fluids*, 22:20, 1979.

[52] H. Mobus, P. Gerlinger, and D. Bruggemann. Comparison of Eulerian and Lagrangian Monte Carlo PDF method for turbulent diffusion flames. *Combustion and Flame*, 124:519–534, 2001.

[53] W. P. Jones and R. Weerasinghe. Probability density function modeling of an axisymmetric combustion chamber. In C. Dopazo, editor, *Advances in turbulence VIII*, page 497, 2000.

[54] V. Raman, H. Pitsch, and R. O. Fox. Eulerian transported probability density function sub-filter model for large-eddy simulation of turbulent combustion. *Combustion Theory and Modeling*, 10(3):439–458, 2006.

[55] D. Roekaerts. Use of a Monte Carlo PDF method in a study of the influence of turbulent fluctuations on selectivity in a jet-stirred reactor. *Applied Scientific Research*, 48:271, 1991.

[56] R. Mustata, L. Valiño, C. Jiménez, WP Jones, and S. Bondi. A probability density function eulerian monte carlo field method for large eddy simulations: application to a turbulent piloted methane/air diffusion flame (Sandia D). *Combustion and Flame*, 145(1-2):88–104, 2006.

[57] Metin Muradoglu, Patrick Jenny, Stephen B. Pope, and David A. Caughey. A consistent hybrid finite-volume/particle method for the PDF equa-

tions of turbulent reactive flows. *Journal of Computational Physics*, 154:342–371, 1999.

[58] B. J. Delarue and S. B. Pope. Application of PDF methods to compressible turbulent flows. *Physics of Fluids*, 9:2704–2715, 1997.

[59] J. Xu and S. B. Pope. PDF calculations of turbulent nonpremixed flames with local extinction. *Combustion and Flame*, 123:281–307, 2000.

[60] Daniele L. Marchisio and Rodney O. Fox. Solution of population balance equations using the direct quadrature method of moments. *Journal of Aerosol Science*, 36:43–73, 2005.

[61] V. Raman and H. Pitsch. LES-FDF simulation of turbulent combustion. In *Proceedings of the 4th Joint Meeting of US Sections of the Combustion Institute*, 2005.

[62] Q. Tang, W. Zhao, M. Bockelie, and R. O. Fox. Multi-environment probability density function method for modelling turbulent combustion using realistic chemical kinetics. *Combustion Theory and Modelling*, 11(6):889–907, Dec 2007.

[63] R McGraw. Description of aerosol dynamics by the quadrature method of moments. *Aerosol Science and Technology*, 27(2):255–265, 1997.

[64] R. G. Gordon. Error Bounds in Equilibrium Statistical Mechanics. *Journal of Mathematical Physics*, 9(5):655–663, 1968.

[65] S. Chapra and R. Canale. *Turbulent Combustion*. McGraw-Hill, 1998.

[66] R. Fan, D. L. Marchisio, and R. O. Fox. Application of the direct quadrature method of moments to polydisperse gas-solid fluidized beds. *Powder Technology*, 139:7–20, 2004.

[67] Peter J. Attar and Prakash Vedula. Direct quadrature method of moments solution of the fokker-planck equation. *Journal of Sound and Vibration*, 317(1-2):265 – 272, 2008.

[68] R. O. Fox and V. Raman. A multienvironment conditional probability density function model for turbulent reacting flows. *Physics of Fluids*, 16(12):4551–4565, 2004.

[69] Jethro Akroyd, Alastair J. Smith, Laurence R. McGlashan, and Markus Kraft. Numerical investigation of DQMoM-IEM as a turbulent reaction closure. *Chemical Engineering Science*, 65(6):1915 – 1924, 2010.

[70] Sanjeeb T. Bose, Parviz Moin, and Donghyun You. Grid-independent large-eddy simulation using explicit filtering. *Physics of Fluids*, 22(10):105103, 2010.

[71] Fotini Katopodes Chow and Parviz Moin. A further study of numerical errors in large-eddy simulations. *Journal of Computational Physics*, 184(2):366 – 380, 2003.

[72] C. M. Kaul, V. Raman, G. Balarac, and H. Pitsch. Numerical errors in the computation of subfilter scalar variance in large eddy simulations. *Physics of Fluids*, 21(5):055102, 2009.

[73] C. M. Kaul and V. Raman. A posteriori analysis of numerical errors in subfilter scalar variance modeling for large eddy simulation. *Physics of Fluids*, 23(3):035102, 2011.

[74] O. Desjardins, R.O. Fox, and P. Villedieu. A quadrature-based moment method for dilute fluid-particle flows. *Journal of Computational Physics*, 227(4):2514 – 2539, 2008.

[75] S. de Chaisemartin, L. Freret, D. Kah, F. Laurent, R.O. Fox, J. Reveillon, and M. Massot. Eulerian models for turbulent spray combustion with polydispersity and droplet crossing. *Comptes Rendus Mecanique*, 337(6-7):438 – 448, 2009.

[76] D. Kah, F. Laurent, L. Freret, S. de Chaisemartin, R. Fox, J. Reveillon, and M. Massot. Eulerian quadrature-based moment models for dilute polydisperse evaporating sprays. *Flow, Turbulence and Combustion*, 85:649–676, 2010.

[77] R.O. Fox. A quadrature-based third-order moment method for dilute gas-particle flows. *Journal of Computational Physics*, 227(12):6313 – 6350, 2008.

[78] R.O. Fox. Higher-order quadrature-based moment methods for kinetic equations. *Journal of Computational Physics*, 228(20):7771 – 7791, 2009.

[79] B.P. Leonard. A stable and accurate convective modelling procedure based on quadratic upstream interpolation. *Computer Methods in Applied Mechanics and Engineering*, 19(1):59 – 98, 1979.

[80] Douglas L. Wright. Numerical advection of moments of the particle size distribution in Eulerian models. *Journal of Aerosol Science*, 38(3):352 – 369, 2007.

[81] G-S. Jiang and C-W. Shu. Efficient implementation of weighted ENO schemes. *Journal of Computational Physics*, 126:202–228, 1996.

[82] M. Herrmann, G. Blanquart, and V. Raman. A bounded quick scheme for preserving scalar bounds in large-eddy simulations. *AIAA Journal*, 44(12):2879–2880, 2006.

[83] V. Vikas, Z.J. Wang, A. Passalacqua, and R.O. Fox. Realizable high-order finite-volume schemes for quadrature-based moment methods. *Journal of Computational Physics*, 230(13):5328 – 5352, 2011.

[84] Heeseok Koo and Venkat Raman. Detailed numerical simulations of a supersonic inlet-isolator. In *Sixth International Symposium on Turbulence and Shear Flow Phenomena, Seoul, Korea*, pages 1368 – 1373, 2009.

[85] H. Koo and V. Raman. Large-Eddy Simulation of a Supersonic Inlet-Isolator. *AIAA Journal*, 50:1596–1613, July 2012.

[86] H. Koo. *Large-Eddy Simulations of Scramjet Engines*. PhD Thesis, The University of Texas at Austin, 2011.

[87] J. S. Evans, C. J. Schexnayder, Jr., and H. L. Beach, Jr. Application of a two-dimensional parabolic computer program to prediction of turbulent reacting flows. *NASA STI/Recon Technical Report N*, 78:20463, March 1978.

[88] M. Mueller, T. Kim, R. Yetter, and F. Dryer. Flow reactor studies and kinetic modeling of the H-2/O-2 reaction. *International Journal of Chemical Kinetics*, 31:113–125, 1999.

[89] Michael E. Mueller and Heinz Pitsch. Large eddy simulation subfilter modeling of soot-turbulence interactions. *Physics of Fluids*, 23(11):115104, 2011.

[90] R.P. Lindstedt and S.A. Louloudi. Joint-scalar transported pdf modeling of soot formation and oxidation. *Proceedings of the Combustion Institute*, 30(1):775 – 783, 2005.

[91] Abhilash J. Chandy, David J. Glaze, and Steven H. Frankel. A Hybrid Large Eddy Simulation/Filtered Mass Density Function for the Calculation of Strongly Radiating Turbulent Flames. *Journal of Heat Transfer - Transactions of the ASME*, 131(5), May 2009.

[92] Jrg Appel, Henning Bockhorn, and Michael Frenklach. Kinetic modeling of soot formation with detailed chemistry and physics: laminar premixed flames of C2 hydrocarbons. *Combustion and Flame*, 121(12):122 – 136, 2000.

[93] Hai Wang and Michael Frenklach. A detailed kinetic modeling study of aromatics formation in laminar premixed acetylene and ethylene flames. *Combustion and Flame*, 110(12):173 – 221, 1997.

[94] Michael Frenklach. Reaction mechanism of soot formation in flames. *Phys. Chem. Chem. Phys.*, 4:2028–2037, 2002.

[95] Andrea DAnna. Combustion-formed nanoparticles. *Proceedings of the Combustion Institute*, 32(1):593 – 613, 2009.

[96] K. Narayanaswamy, G. Blanquart, and H. Pitsch. A consistent chemical mechanism for oxidation of substituted aromatic species. *Combustion and Flame*, 157(10):1879 – 1898, 2010.

[97] Michael E. Mueller and Heinz Pitsch. LES model for sooting turbulent nonpremixed flames. *Combustion and Flame*, 159(6):2166 – 2180, 2012.

[98] R.W. Bilger. The structure of turbulent nonpremixed flames. *Symposium (International) on Combustion*, 22(1):475 – 488, 1989.

[99] Matthias Ihme and Heinz Pitsch. Modeling of radiation and nitric oxide formation in turbulent nonpremixed flames using a flamelet/progress variable formulation. *Physics of Fluids*, 20(5):055110, 2008.

[100] Guillaume Blanquart and Heinz Pitsch. A joint volume-surface-hydrogen multi-variate model for soot formation. In *Combustion Generated Fine Carbonaceous Particles*, pages 437–463. Karlsruhe University Press, 2009.

[101] M.E. Mueller, G. Blanquart, and H. Pitsch. Modeling the oxidation-induced fragmentation of soot aggregates in laminar flames. *Proceedings of the Combustion Institute*, 33(1):667 – 674, 2011.

[102] M. E. Mueller, G. Blanquart, and H. Pitsch. Hybrid method of moments for modeling soot formation and growth. *Combustion and Flame*, 156:1143–1155, 2009.

[103] Michael Frenklach. Method of moments with interpolative closure. *Chemical Engineering Science*, 57(12):2229 – 2239, 2002.

[104] S. James, J. Zhu, and M. S. Anand. Lagrangian PDF transport method for simulations of axisymmetric turbulent reacting flows. In *43rd AIAA Aerospace Sciences Meeting and Exhibit*, number 156, 2005.

[105] H. Pitsch, E. Riesmeier, and N. Peters. Unsteady flamelet modeling of soot formation in turbulent diffusion flames. *Combustion science and technology*, 158:389–406, 2000.

[106] Y. Liu and R. O. Fox. CFD predictions for chemical processing in a confined impinging-jets reactor. *AIChE Journal*, 52:731, 2006.

[107] Charles D. Pierce. *Progress-variable approach for large-eddy simulation of turbulence combustion*. PhD thesis, Stanford University, 2001.

[108] K. Akselvoll and P. Moin. Large eddy simulation of turbulent confined coannular jets. *Journal of Fluid Mechanics*, 315:387–411, 1996.

[109] Olivier Desjardins, Guillaume Blanquart, Guillaume Balarac, and Heinz Pitsch. High order conservative finite difference scheme for variable density low mach number turbulent flows. *Journal of Computational Physics*, 227:7125–7159, 2008.

[110] T.W.J. Peeters, P.P.J. Stroomer, J.E. de Vries, D.J.E.M. Roekaerts, and C.J. Hoogendoorn. Comparative experimental and numerical investigation of a piloted turbulent natural-gas diffusion flame. *Symposium (International) on Combustion*, 25(1):1241 – 1248, 1994.

[111] P.A. Nooren, M. Versluis, T.H. van der Meer, R.S. Barlow, and J.H. Frank. Raman-rayleigh-lif measurements of temperature and species concentrations in the delft piloted turbulent jet diffusion flame. *Applied Physics B: Lasers and Optics*, 71:95–111, 2000.

[112] P.P.J. Stroomer, J.E. de Vries, and Th.H. van der Meer. Effects of small- and large-scale structures in a piloted jet diffusion flame. *Flow, Turbulence and Combustion*, 62:53–68, 1999.

[113] H. Pitsch. A C++ computer program for 0-d and 1-d laminar flame calculations. RWTH Aachen, 1998.

[114] Fabrizio Bisetti, Guillaume Blanquart, Michael E. Mueller, and Heinz Pitsch. On the formation and early evolution of soot in turbulent nonpremixed flames. *Combustion and Flame*, 159(1):317 – 335, 2012.

[115] Stephen B. Pope. Self-conditioned fields for large-eddy simulations of turbulent flows. *Journal of Fluid Mechanics*, 652:139–169, JUN 10 2010.

[116] D.O. Lignell, J.C. Hewson, and J.H. Chen. A-priori analysis of conditional moment closure modeling of a temporal ethylene jet flame with soot formation using direct numerical simulation. *Proceedings of the Combustion Institute*, 32(1):1491–1498, 2009.

[117] R. Mcdermott and S. B. Pope. A particle formulation for treating differential diffusion in filtered density function methods. *Journal of Computational Physics*, 226(1):947–993, 2007.

[118] Edward S. Richardson and Jacqueline H. Chen. Application of PDF mixing models to premixed flames with differential diffusion. *Combustion and Flame*, 159(7):2398 – 2414, 2012.

[119] S. M. Ross. *Introduction to Probability and Statistics for Engineers and Scientists*. Burlington : Elsevier Science, 2009.